Featured in Physics

Enhanced Quantum Control of Individual Ultracold Molecules Using Optical Tweezer Arrays

Daniel K. Ruttley,[1,2] Alexander Guttridge,[1,2] Tom R. Hepworth,[1,2] and Simon L. Cornish[1,2,*]

[1] *Department of Physics, Durham University, South Road, Durham DH1 3LE, United Kingdom*

[2] *Joint Quantum Centre Durham-Newcastle, Durham University, South Road, Durham DH1 3LE, United Kingdom*

(Received 30 January 2024; accepted 8 March 2024; published 13 May 2024)

Control over the quantum states of individual molecules is crucial in the quest to harness their rich internal structure and dipolar interactions for applications in quantum science. In this paper, we develop a toolbox of techniques for the control and readout of individually trapped polar molecules in an array of optical tweezers. Starting with arrays of up to eight Rb and eight Cs atoms, we assemble arrays of RbCs molecules in their rovibrational and hyperfine ground state with an overall efficiency of 48(2)%. We demonstrate global microwave control of multiple rotational states of the molecules and use an auxiliary tweezer array to implement site-resolved addressing and state control. We show how the rotational state of the molecule can be mapped onto the position of Rb atoms and use this capability to readout multiple rotational states in a single experimental run. Further, using a scheme for the midsequence detection of molecule formation errors, we perform rearrangement of assembled molecules to prepare small defect-free arrays. Finally, we discuss a feasible route to scaling to larger arrays of molecules.

DOI: 10.1103/PRXQuantum.5.020333

I. INTRODUCTION

Ultracold molecules offer a versatile platform for quantum science [1–3], with applications spanning quantum simulation [4–9] and quantum information processing [10–16] to ultracold chemistry [17–19] and precision measurement [20–24]. Molecules feature a rich internal structure, constituting a ladder of rotational states with long radiative lifetimes. Preparing molecules in a superposition of rotational states engineers dipole-dipole interactions that can be controlled using microwave fields. These properties make rotational states well suited for applications as qubits [25,26] or pseudospins in a quantum simulator [27–29]. Moreover, the abundance of long-lived rotational states unlocks possibilities such as synthetic dimensions in the rotational degree of freedom [30], realization of qudits [16], or the implementation of quantum error-correcting codes in the molecule's internal states [15].

Realization of many of these theoretical proposals demands a high level of control of the quantum states of individual molecules. Attaining such control is pivotal to exploit the wide array of tools offered by ultracold molecules for quantum science. Significant progress has been made in preparing and manipulating internal and external states of molecules [31,32] but control and detection of individual molecules in a single internal and external quantum state is an ongoing challenge.

Optical tweezer arrays are a powerful platform for the trapping, control, and readout of single ultracold particles [33–35]. Arrays of tweezers are dynamically reconfigurable, allowing flexible connectivity [36] and enabling the preparation of states with low configurational entropy through rearrangement of particles [37–39]. In this tweezer array platform, long-range interactions between trapped particles have been utilized to simulate complex quantum systems [40–42]. The platform's inherent scalability [43] provides a promising avenue for constructing arrays with an even greater number of particles.

The extension of tweezer arrays to ultracold molecules has been realized recently for both laser-cooled [44–46] and assembled molecules [47,48]. For neutral atom tweezer arrays a range of experimental techniques have been demonstrated, including rearrangement [38,39], erasure conversion [49,50], and midcircuit operations [51–54]. In this work, we develop a similar toolbox of techniques for the control and readout of ultracold bialkali molecules trapped in arrays of optical tweezers. Specifically, we globally and locally control multiple rotational states of individually trapped ultracold molecules. We introduce a technique for the readout of multiple rotational states in a single iteration of the experiment,

*Corresponding author. s.l.cornish@durham.ac.uk

Published by the American Physical Society under the terms of the Creative Commons Attribution 4.0 International license. Further distribution of this work must maintain attribution to the author(s) and the published article's title, journal citation, and DOI.

achieved by mapping onto atomic states, and demonstrate rearrangement of molecules using midsequence detection of formation errors.

The structure of the paper is as follows. Section II gives an overview of our experimental platform. Section III describes our procedure for the assembly of molecules in optical tweezers and reports the efficiency of this process. Section IV demonstrates global control of the rotational states of molecules in our optical tweezer array using microwave fields to perform coherent multiphoton excitation. Section V describes the detection of multiple rotational states of molecules in a single experimental run. Section VI demonstrates local control of rotational states using an addressing tweezer in combination with microwave fields to selectively excite specific molecules in the array. Section VII describes the detection of molecule formation errors and rearrangement of molecules to prepare a defect-free array. Finally, Sec. VIII examines the prospects for scaling the techniques described in this paper to larger arrays.

II. OVERVIEW OF THE EXPERIMENTAL PLATFORM

Figure 1(a) shows an overview of the experimental apparatus [55,56] we use to produce ultracold $^{87}Rb^{133}Cs$ (hereafter RbCs) molecules trapped in one-dimensional arrays of optical tweezers. A key aspect of our experimental setup is the use of two distinct wavelengths of optical tweezers, which enables species-specific trapping and independent control of the atoms and molecules. Tweezers at a wavelength of 1066 nm are attractive to all species in our experiment, whereas tweezers at 817 nm are strongly attractive for Rb, weakly attractive for RbCs, and repulsive for Cs. The 1066-nm tweezers are created with a spatial light modulator (SLM) and the 817-nm tweezers are created with a two-dimensional acousto-optic deflector (2D AOD). Both wavelengths are aligned through a high numerical aperture objective lens to generate the tweezers in an ultrahigh vacuum glass cell. The SLM generates a static array whereas, by changing the radiofrequency tones applied to the 2D AOD, we can dynamically switch and move the 817-nm tweezers midroutine to manipulate the atoms and molecules.

Molecules are assembled from optical tweezer arrays of individually trapped Rb and Cs atoms [Fig. 1(b)(i)] to form an array of RbCs molecules in the rovibrational ground state [Fig. 1(b)(ii)]. As the molecules are individually trapped we avoid loss caused by molecular collisions [57–60] and are able to selectively control individual molecules. The molecules formed occupy a single internal quantum state and the assembly from laser-cooled atoms produces molecules predominantly in the motional ground state of the optical tweezers. Microwave fields can then be used to manipulate the rotational state of the molecules [Fig. 1(b)(iii)]. The transitions and states that we explore in this work are highlighted in Fig. 1(c).

We exploit individual control of the species in our experiment to readout information. Figure 1(b)(iii) highlights a general scheme for the indirect detection of molecules, whereby an atom-specific tweezer array is used to extract Rb atoms from an array of tweezers that is partially filled with molecules. By measuring the occupancy of this "detection array," we can infer the lack of molecules in the corresponding traps in the primary array. This detection scheme is discussed further in Sec. III D. By imaging these atoms midroutine using the scheme shown in Fig. 1(d), we can detect molecule formation errors and, hence, perform rearrangement of the occupied traps, as discussed in Sec. VII. Alternatively, by repeatedly converting different molecular states to atom pairs and using the Rb extraction method discussed above, we can map the molecular states onto multiple detection arrays for multistate readout, as described in Sec. V.

III. MOLECULE FORMATION

A. Formation of weakly bound molecules

All experiments begin by stochastically loading individual Rb and Cs atoms in arrays of optical tweezers at wavelengths 817 nm and 1066 nm, respectively. The atoms are imaged with fidelity >99.9% [55] and dynamically rearranged to create defect-free one-dimensional arrays with up to eight atoms of each species, as illustrated in Fig. 1(b)(i). Following this, the atoms are prepared predominantly in the motional ground state using Raman sideband cooling and transferred to the hyperfine state $(f = 1, m_f = 1)_{Rb}(f = 3, m_f = 3)_{Cs}$ [56]. The arrays are then merged along the interarray axis to generate atom pairs confined in the 1066-nm array. The merging is carefully optimized to minimize heating such that the atom pairs predominantly occupy the ground state of relative motion. We find that the atom pairs are successfully prepared in the ground state of relative motion in 56(5)% of experimental runs. The infidelity in the initial preparation of each species in the correct hyperfine state is approximately 1% prior to merging. However, significant Raman scattering of Rb caused by the 817-nm tweezer during the merging process means that atom pairs in the correct hyperfine state are prepared in 93(2)% of runs. The remaining 7(2)% of atom pairs are prepared in excited hyperfine states and, for the duration of typical experimental routines, are lost due to inelastic collisions following merging.

Molecule formation is achieved in two steps. We first utilize an interspecies Feshbach resonance to magnetoassociate atom pairs into molecules [48,61]. The molecules are then transferred from the weakly bound state $|F\rangle$ to the rovibrational ground state $|G\rangle$ using two-photon stimulated Raman adiabatic passage (STIRAP) following the

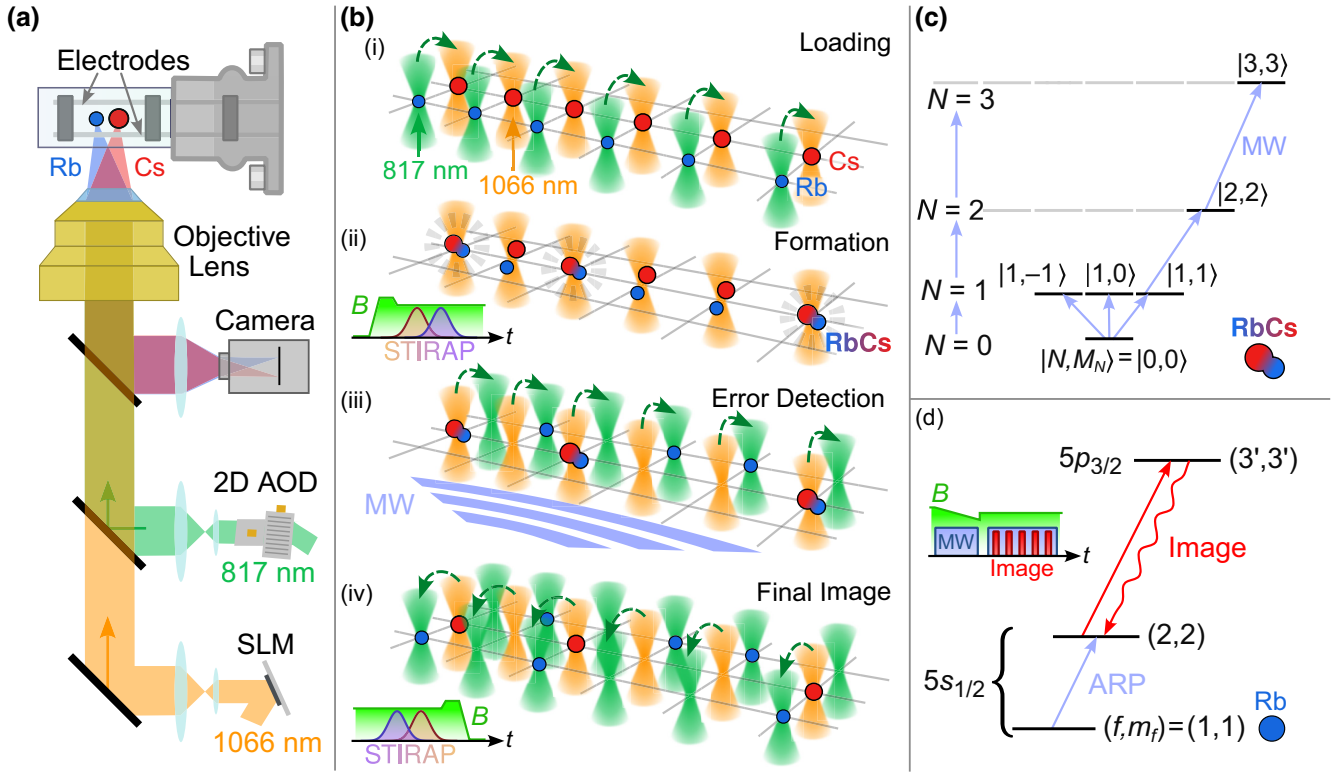

FIG. 1. Overview of the experimental apparatus and methodology for creating, controlling and detecting ultracold RbCs molecules. (a) The simplified setup showing the vacuum cell, objective lens, and key elements of the optical setup. Arrays of 1066-nm tweezers are created with a spatial light modulator (SLM). Arrays of 817-nm tweezers are created with a two-dimensional acousto-optic deflector (2D AOD). Trapped atoms are detected by imaging atomic fluorescence onto a camera. (b) Stages of a typical experiment. (b)(i) Initially Rb and Cs atoms are loaded and rearranged to prepare defect-free one-dimensional arrays in species-specific tweezers. (b)(ii) The Rb tweezers are merged to overlap with the Cs tweezers. The atom pairs are magnetoassociated and the resultant molecules are transferred to the ground state using stimulated Raman adiabatic passage (STIRAP), as illustrated in the inset. (b)(iii) Atom pairs remaining due to failed molecule formation are separated. The Cs is ejected and the Rb is stored in a separate row of tweezers. Detection of the Rb atom indicates failure to form a molecule in a particular site. An experiment is performed on the molecules using microwaves to address rotational transitions. (iv) Finally the molecules are dissociated and the resulting atom pairs are separated into their original traps for imaging. (c) The lowest-energy rotational levels of RbCs labeled with the rotational angular momentum N and its projection M_N. Arrows indicate the microwave transitions used in this work. (d) Energy levels used in imaging of Rb at high magnetic field. The closed cycle $(f = 2, m_f = 2) \rightarrow (3', 3')$ is used for imaging the atom at high field; the transfer $(1, 1) \rightarrow (2, 2)$ is performed with adiabatic rapid passage (ARP).

scheme illustrated in Fig. 2(a). The energy pathway used to access state $|F\rangle$ from the atom pair state is shown in Fig. 2(b). Starting at a magnetic field of 205.8 G, atom pairs are adiabatically transferred into a near-threshold molecular state $|s\rangle$ by ramping the magnetic field over an interspecies Feshbach resonance at 197.1 G. The magnetic field is then lowered further to traverse an avoided crossing associated with a Feshbach resonance at approximately 182 G, transferring the molecules to state $|F\rangle$ at a field of 181.699(1) G.

Only atom pairs in the required hyperfine state and the ground state of relative motion can be magnetoassociated to form a molecule [61,62]. We measure the conversion efficiency from atom pairs to molecules in state $|F\rangle$ by inducing state-sensitive loss of molecules [48]. By applying a 1-ms pulse of resonant "pump" light at 1557 nm, we excite molecules in state $|F\rangle$ to state $|E\rangle$ from which they may decay to other states by spontaneous emission. When this happens we do not recover atom pairs following the reversal of the association ramps [48]. This allows us to optimize the parameters of the magnetoassociation sequence by measuring the probability to lose the atom pair.

Figure 2(c) shows the result of such a measurement where we vary the magnetic field ramp speed dB/dt during the magnetoassociation sweep across the Feshbach resonance at 197.1 G. At high dB/dt, the avoided crossing between the atom pair and molecule states is traversed diabatically and molecules are not formed. The pump light then has no effect and atom pairs are recovered at the end of the sequence in 97(1)% of experimental runs. Here the background loss of 3(1)% is from atom pairs that

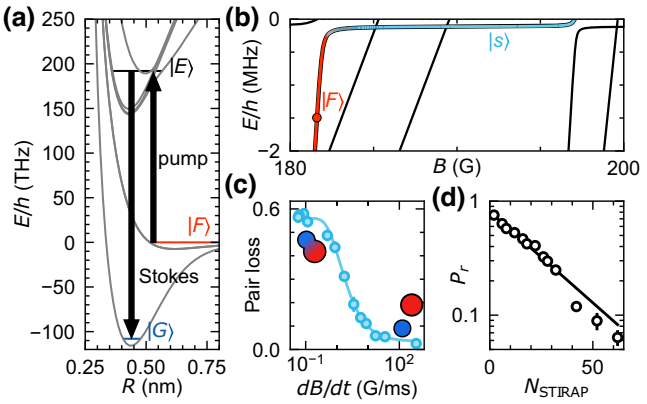

FIG. 2. (a) Electronic energy structure of RbCs molecules highlighting the STIRAP pathway connecting the Feshbach state $|F\rangle$ to the ground state $|G\rangle$. (b) Near-threshold molecular bound states and the pathway for magnetoassociation. Atom pairs are associated into the near-threshold state $|s\rangle$ (blue) by sweeping the magnetic field down across the Feshbach resonance at 197.1 G. The magnetic field is then decreased further to transfer the molecules into state $|F\rangle$ (red) at 181.7 G. (c) Probability of losing an atom pair as a function of the magnetic field ramp speed dB/dt over the avoided crossing at 197.1 G. Molecule loss is induced by subsequently sweeping the magnetic field to 181.7 G and applying pump light. (d) Efficiency of STIRAP as a function of the number of one-way STIRAP transfers, N_{STIRAP}. We extract a one-way efficiency of 96.4(1)% from the fitted solid line.

occupy an excited hyperfine state. This is lower than the 7(2)% infidelity in the hyperfine state preparation mentioned above, as in this measurement the atom pairs are held for a shorter time such that the collisional loss does not saturate. When a slower magnetic field ramp is used, we adiabatically transfer to $|s\rangle$ then subsequently to $|F\rangle$ and molecules are lost once the pump light is applied.

The solid line in Fig. 2(c) shows the result of fitting a Landau-Zener model to the data, where the probability of traversing the avoided crossing adiabatically is $p = 1 - \exp(-(4\pi^2 n_2 \hbar/2\mu)|a_s \Delta/(dB/dt)|)$ [63–65]. Here μ is the reduced mass of the two atoms, $a_s = 645(60)a_0$ is the background s-wave scattering length and $\Delta = 90(10)$ mG is the width of the Feshbach resonance [66]. We scale p to match the experimental contrast in the atom-pair loss and add a small offset to account for the experimental background. Accordingly, the free parameters in our model are the atom-pair density n_2 and the probability of atom-pair loss in the limits of large and small dB/dt. From this model we extract $n_2 = 1.7(1) \times 10^{13}$ cm^{-3}. When dB/dt is large enough to make the adiabatic conversion probability negligible, the probability of atom-pair loss is equal to the background loss value of 3(1)%. As dB/dt is decreased, corresponding to a more adiabatic ramp, the observed atom-pair loss is the sum of the background loss and the loss of formed molecules. In the small dB/dt limit, p saturates and we fit the atom-pair loss to be 56(1)%, corresponding to a molecule formation efficiency of 53(1)%. Magnetoassociation requires atom pairs in the ground hyperfine state *and* the ground state of relative motion. The probabilities for preparing atom pairs in these states are 93(2)% and 56(5)%, respectively. Therefore, for sufficiently slow magnetic field ramps, we expect to convert an atom pair to a molecule in 52(5)% of experimental runs, which is in excellent agreement with the fitted conversion efficiency. For the rest of this work, we use sufficiently small dB/dt to saturate p such that we expect that over 99% of atom pairs in the correct states are transferred adiabatically to the molecular state $|F\rangle$.

B. Transfer to molecular ground state

We transfer molecules in state $|F\rangle$ to the rovibrational ground state of the $X^1\Sigma^+$ potential using a two-photon stimulated Raman adiabatic passage (STIRAP) process [67,68]. We populate the hyperfine ground state $|G\rangle \equiv |N = 0, M_N = 0, m_{\mathrm{Rb}} = 3/2, m_{\mathrm{Cs}} = 7/2\rangle$ at a magnetic field of 181.699(1) G [57,69–72]. Here, N is the rotational angular momentum quantum number and M_N is its projection along the quantization axis. m_{Rb} (m_{Cs}) is the projection of the nuclear spin $i_{\mathrm{Rb}} = 3/2$ ($i_{\mathrm{Cs}} = 7/2$) of Rb (Cs) along the quantization axis. The state $|G\rangle$ is the lowest energy hyperfine state for magnetic fields above approximately 90 G and conveniently, being a spin-stretched state, has well-defined nuclear-spin projections [73].

The STIRAP process uses the "pump" beam ($\lambda = 1557$ nm) and a "Stokes" beam ($\lambda = 977$ nm) that together couple state $|F\rangle$ to state $|G\rangle$ via the electronically excited state $|E\rangle$ [57,69], as shown in Fig. 2(a). The intensities of these beams are modulated with the so-called "counter-intuitive" pulse sequence [67] over 70 μs, during which the dark state adiabatically evolves from state $|F\rangle$ to state $|G\rangle$. Further details of the STIRAP setup are given in Appendix A.

C. Molecule detection scheme

The lack of closed optical cycling transitions in RbCs precludes scattering enough photons for single-molecule fluorescence detection. Instead we map the success or failure of molecule formation onto atoms in specific tweezers and then use standard atomic fluorescence imaging of Rb and Cs, as described below.

We utilize a technique similar to erasure conversion in neutral-atom arrays [50] to detect sites of the array in which molecule formation failed. Formation errors result in atom pairs remaining in the 1066-nm tweezers after the molecules have been transferred to state $|G\rangle$, as shown in Fig. 1(b)(ii). We detect these errors by pulling out the remaining Rb atoms and storing them in a separate row of 817-nm tweezers (the "detection array"), as shown

in Fig. 1(b)(iii). In addition, we apply resonant light to remove any remaining Cs atoms.

Subsequently, we also reverse the STIRAP sequence to transfer molecules back to state $|F\rangle$ before immediately reversing the association field ramps to convert the molecules back to atom pairs. The resulting atom pairs are then separated by pulling out the Rb atoms and returning them to their original traps, as shown in Fig. 1(b)(iv).

Finally, at the end of the experimental run we take a fluorescence image of Rb and Cs to determine the occupancy of the *three* tweezer arrays: the original arrays containing atoms recovered from the molecules *and* the detection array containing Rb atoms in sites where molecule formation failed.

From the final fluorescence image we determine the recovery probability P_r of the molecules as follows. Firstly, the presence of a Rb atom in the detection array indicates that molecule formation failed in the corresponding 1066-nm trap and we ignore that site when analyzing statistics. Conversely, if the detection trap is empty, we assume that a molecule was formed in that site and therefore consider the occupancy of the corresponding initial Rb and Cs traps. A molecule is then deemed to be "recovered" if both atoms that formed it are successfully imaged in their original traps at the end of a routine. Thus P_r is defined as the probability that we recover both a Rb and a Cs atom in their initial traps, ignoring sites in which the presence of a Rb atom in the detection array indicates that molecule formation failed.

D. Molecule formation and detection efficiencies

The efficiency of molecule formation (and subsequent recovery) is primarily limited by the STIRAP transfer efficiency and the loss of molecules in state $|F\rangle$. We quantify these losses below using the detection scheme described in Sec. III C above.

We measure the one-way STIRAP efficiency by repeating many round trips $|F\rangle \rightarrow |G\rangle \rightarrow |F\rangle$ before reversing the association field ramps and measuring the molecule recovery probability. The results are shown in Fig. 2(d). From this measurement we extract a one-way transfer efficiency of 96.4(1)%, assuming the efficiency of the forward ($|F\rangle \rightarrow |G\rangle$) and reverse ($|G\rangle \rightarrow |F\rangle$) transfers to be the same. This is marginally better than the efficiencies reported for RbCs in bulk gases [57,71] and comparable to the highest reported efficiencies for ground-state transfer of diatomic molecules [29,74].

Figure 3 shows lifetime measurements of the molecular states $|F\rangle$ and $|G\rangle$ for different tweezer intensities. We find that molecules in the weakly bound state $|F\rangle$ exhibit a much larger loss rate than ground-state molecules. We have previously observed a photoassociation resonance from state $|F\rangle$ at 1063.91(7) nm with an estimated transition dipole moment (TDM) of $0.064(2) \times ea_0$ [75]. We

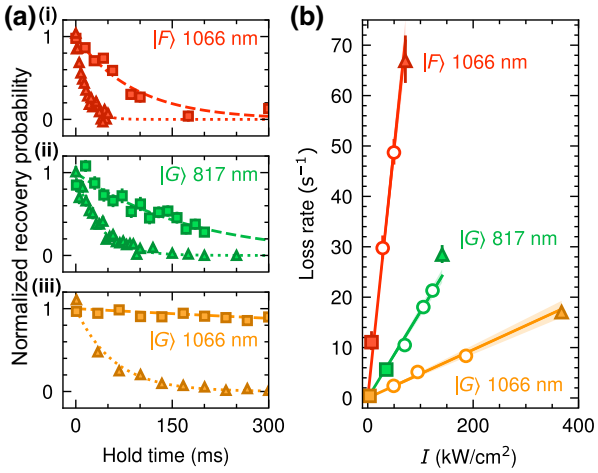

FIG. 3. Lifetime of RbCs molecules in optical tweezers with wavelengths of 1066 nm and 817 nm. (a) Normalized recovery probabilities as a function of the hold time in the tweezers for molecules (i) in state $|F\rangle$ and 1066 nm, (ii) the ground state $|G\rangle$ and 817 nm, and (iii) the ground state $|G\rangle$ and 1066 nm. In each panel results are shown for two different intensities with the values indicated by the corresponding symbols in (b). The axes have been rescaled to make the contrast of the fits equal to unity. The gold squares in (iii) show the loss of molecules in state $|G\rangle$ at our typical operating intensity. (b) Scaling of the molecule loss rates with tweezer intensity (I). The solid lines show linear fits to the measured loss rates.

believe that the tweezer light is driving a transition from the $a^3\Sigma^+$ manifold to the $c^3\Sigma^+$ manifold [76]. To reduce the loss rate from photon scattering in the wings of this resonance, we operate the molecule tweezers at a wavelength of 1065.512 nm. At this wavelength, we determine the loss rate of molecules in state $|F\rangle$ to be 0.99(4) $s^{-1}/(kW/cm^2)$ from the fit to the red points in Fig. 3(b). To mitigate this loss, we operate at low tweezer intensities and minimize the time between the molecule entering state $|F\rangle$ and being transferred to state $|G\rangle$. Unfortunately, the narrow (approximately 100 kHz) linewidths of the STIRAP transitions necessitate a 10 ms hold following the magnetoassociation ramps to achieve sufficient magnetic field stability (approximately 50 mG) for efficient transfer. During this time the molecules in state $|F\rangle$ are held in tweezers with an intensity of 6 kW/cm^2 such that 5(1)% are lost. We note that the molecular state $|s\rangle$ shown in Fig. 2(b) that is populated in the initial magnetoassociation ramp has a much longer lifetime, consistent with that of the atom pair (>10 s). However, STIRAP from this state is inefficient due to the weak coupling to state $|E\rangle$.

The loss rate of molecules in the ground state $|G\rangle$ is much lower than that of molecules in state $|F\rangle$. From the fits in Fig. 3(b), we determine loss rates for state $|G\rangle$ of 0.171(8) $s^{-1}/(kW/cm^2)$ in tweezers with a wavelength of 816.848 nm and 0.047(4) $s^{-1}/(kW/cm^2)$ for a wavelength of 1065.512 nm. The linear relation observed between loss

TABLE I. Efficiencies of each stage of the molecule formation. The values are measured experimentally unless stated otherwise.

Experimental stage	Efficiency
Preparation of atom-pair hyperfine state	0.93(2)
Occupancy of ground state of relative motion (following the merging of the traps)	0.56(5)
Magnetoassociation efficiency (calculated)	>0.99
Atom pair → $\|F\rangle$ conversion	**0.53(1)**
$\|F\rangle$ survival pre-STIRAP	0.95(1)
STIRAP transfer $\|F\rangle \rightarrow \|G\rangle$	0.964(1)
$\|F\rangle \rightarrow \|G\rangle$ conversion (calculated)	**0.91(1)**
Atom pair → $\|G\rangle$ conversion (calculated)	**0.48(2)**

rate and intensity suggests that the lifetime is limited by photon scattering of the tweezer light, most likely Raman scattering. A single Raman-scattering event would appear as loss since we detect only molecules in the specific rotational and hyperfine state addressed by the STIRAP lasers. In light of this, we typically operate the tweezers at a low intensity where the lifetime of state $|G\rangle$ is typically 2.7(4) s, corresponding to the gold squares in Fig. 3(a)(iii), and loss is negligible for the duration of most experiments. This lifetime is still limited by scattering of the trapping light; the vacuum lifetime of atoms in the experiment is > 30 s [77].

The efficiencies of each step of the molecule formation protocol are summarized in Table I. We successfully convert atom pairs to molecules in state $|F\rangle$ with an efficiency of 53(1)%, limited by the initial state preparation of the atom pairs. Subsequently, 91(1)% of the molecules in state $|F\rangle$ are successfully transferred to the ground state $|G\rangle$. The overall efficiency for the conversion of an atom pair to a rovibrational ground-state molecule is therefore 48(2)%.

The maximum probability of molecule recovery that we measure is $P_r = 75(1)\%$. This corresponds to the value after a single round-trip STIRAP in Fig. 2(d). If our scheme for detecting molecule formation was perfect, we would expect to measure 88(1)%, limited by the lifetime of state $|F\rangle$ and the infidelity of a round-trip STIRAP. However, our detection scheme overestimates molecule formation due to loss of atom pairs prior to magnetoassociation. The overall probability that a detection trap is empty is 60(3)%; a combination of successful molecule formation [53(1)%] and loss of atoms prepared in the wrong hyperfine state [7(2)%]. With our detection scheme, these two events are indistinguishable and we assume that a molecule has been formed in both cases. In reality, a molecule is only formed in 88(3)% of cases where the detection trap is empty. Accounting for this, we would expect to measure $P_r = 77(3)\%$, in agreement with our observations.

IV. GLOBAL CONTROL OF ROTATIONAL STATES

The lowest rotational energy levels in the vibrational ground state of RbCs are shown in Fig. 1(c) where states are labeled with $|N, M_N\rangle$. The energies of the rotational levels are $h \times B_v N(N+1)$ such that the splitting between neighboring rotational manifolds is in the microwave domain (for RbCs, $B_v \approx 490$ MHz) [73]. This picture ignores coupling between the rotational angular momentum and the nuclear spins of the constituent atoms ($i_{\mathrm{Rb}} = 3/2$ and $i_{\mathrm{Cs}} = 7/2$). When optical and magnetic fields are applied, this coupling causes each $|N, M_N\rangle$ state to split into $(2i_{\mathrm{Rb}}+1)(2i_{\mathrm{Cs}}+1) = 32$ hyperfine states. This hyperfine structure is illustrated in Fig. 4(a) for the lowest four rotational states. Here, the energies of the states are shown as a function of the intensity I_{1066} of the 1066-nm tweezer and the magnetic field is 181.699 G. When performing STIRAP we form molecules in the rovibrational and hyperfine ground state $|G\rangle$ (lowest red line). The transitions that we drive between rotational levels are shown by vertical lines.

Transitions between rotational levels are driven using microwave fields to which strong coupling is facilitated by the molecule-frame electric dipole moment (for RbCs, $d_0 = 1.225$ D) [69]. Allowed electric dipole transitions are those with $|\Delta N| = 1$ and $|\Delta M_N| \leq 1$. The strength of the transition is determined by the transition dipole moment (TDM) $\mu_{i,j} = \langle \psi_i | \mu | \psi_j \rangle$, where the components $(\mu^z_{i,j}, \mu^+_{i,j}, \mu^-_{i,j})$ of $\mu_{i,j}$ describe the strength of π, σ^+, and σ^- transitions, respectively. The nuclear spin is not addressed when driving rotational transitions such that we can only couple to hyperfine states with nuclear spins unchanged from those of $|G\rangle$; namely $m_{\mathrm{Rb}} = 3/2$ and $m_{\mathrm{Cs}} = 7/2$. At the operating fields used in this work (approximately 200 G) the molecular eigenstates are generally superpositions of states of different m_{Rb} and m_{Cs}, and the only good quantum numbers that can be used to describe them are N and $M_F \equiv M_N + m_{\mathrm{Rb}} + m_{\mathrm{Cs}}$. The exceptions to this are the stretched states with maximum $|M_F|$; for these states $|m_{\mathrm{Rb}}| = 3/2$, $|m_{\mathrm{Cs}}| = 7/2$ and M_N is a good quantum number. For the work presented here, we drive transitions to either stretched states or hyperfine states with mixed character for which the component with $m_{\mathrm{Rb}} = 3/2$ and $m_{\mathrm{Cs}} = 7/2$ has the largest amplitude. This criterion selects the transitions with the highest TDMs. For simplicity, we continue to label the states $|N, M_N\rangle$, but give the full-state compositions in Appendix B.

We use in-vacuum electrodes mounted inside the glass cell [55] as a microwave antenna to drive coherent transfer between molecular rotational states. These electrodes were designed to orient molecules in the laboratory frame by generating large dc electric fields. The four electrodes are positioned in a 9.6×5.6 mm^2 rectangular array centered around the optical tweezers: this aspect ratio $(\sqrt{3} : 1)$

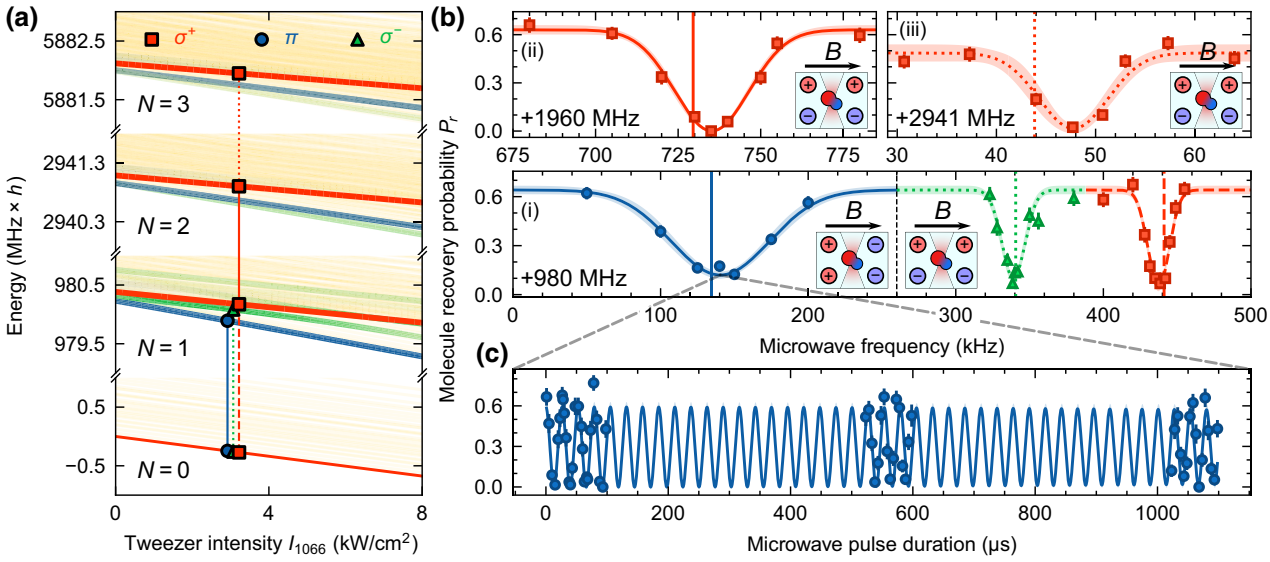

FIG. 4. Excitation of RbCs molecules to higher rotational states. (a) Hyperfine energy structure of the first four rotational manifolds of RbCs as a function of 1066-nm tweezer intensity at a magnetic field of 181.699 G. Energies are given relative to the energy of state $|G\rangle$ in free space. The red lines show the spin-stretched hyperfine states of each manifold, where the molecule is initially prepared in the ground state (lowest red line). σ^+, π, and σ^- transitions from each spin-stretched state are shown in red, blue, and green, respectively. The yellow lines show other hyperfine states that we do not access. The color of the lines represents the TDM of a given transition: more intense lines have higher TDMs. (b) Spectroscopy of the $N = 1, 2, 3$ rotational manifolds for (i),(ii),(iii), respectively, in a 3.07 kW/cm^2 tweezer. Changing the electrode configuration (insets) allows us to drive either π or $\sigma^{\pm}$ transitions. (c) Rabi oscillation on the π transition $|0,0\rangle \rightarrow |1,0\rangle$ for a single trapped molecule.

increases the uniformity of applied fields by eliminating the field curvature along the horizontal axis [78]. We find that the electrodes are a good antenna for the approximately GHz frequency radiation that is resonant with RbCs rotational transitions. The magnetic field, which sets the quantization axis, is applied in the horizontal direction parallel to the long dimension of the rectangular electrode array. An additional external dipole Wi-Fi antenna is mounted approximately 10 cm from the vacuum chamber. Using this external antenna we can also drive transitions, albeit with much reduced polarization control due to the presence of magnetic field coils around the cell.

We demonstrate rotational state control by driving coherent microwave transitions from the rovibrational ground state $|G\rangle$ to higher rotational states. Excitation to higher rotational states is detected by the failure to recover atom pairs from the (excited) molecules at the end of the experimental sequence due to the state specificity of the reverse STIRAP transfer. We selectively drive either $\sigma^{\pm}$ or π transitions by connecting the electrodes in different configurations to change the orientation of the electric field of the microwave radiation. When the electric field is parallel to the applied magnetic field we drive π transitions; when the two fields are orthogonal we drive $\sigma^{\pm}$ transitions.

Figure 4(b)(i) shows spectroscopy from state $|G\rangle$ to the $N = 1$ manifold, with the polarity of the connections to the electrodes shown inset. Here, the magnetic field is 181.699(1) G and the intensity of the 1066-nm tweezer is $I_{1066} = 3.07$ kW/cm^2. We measure the frequencies of the π, σ^-, and σ^+ transitions to be 980.140(2), 980.3391(9), and 980.4374(5) MHz, respectively. The widths of the measured features are transform limited. The vertical lines in Fig. 4(b) show the expected transition frequencies. We calculate these and the state energies shown in Fig. 4(a) by solving the molecular Hamiltonian [79], including the interactions with external optical and magnetic fields. We use the molecular constants determined in previous bulk-gas experiments [73,80,81]. The value of the isotropic polarizability $\alpha^{(0)}$ is scaled from that measured by Blackmore *et al.* [82] to account for the difference in trapping wavelengths [83]; here we use $\alpha^{(0)}_{1066} = 2000 \times 4\pi\varepsilon_0 a_0^3$. By measuring the frequency of the π transition in 1065.512-nm tweezers of different intensities I_{1066}, we determine the anisotropic polarizability $\alpha^{(2)}_{1066} = 1980(60) \times 4\pi\varepsilon_0 a_0^3$. The measured transition frequencies are within 10 kHz of the calculated values; we expect that the discrepancy between the two is primarily caused by our simplifying assumption that the polarization of the tweezer is exactly aligned to the quantization axis of the magnetic field.

We observe coherent oscillations between states by changing the duration of the applied microwave pulses. For example, in Fig. 4(c) we show the effect of changing

the pulse length with the microwave frequency set to that of the π transition $|0,0\rangle \rightarrow |1,0\rangle$ for a single trapped molecule. With a small rf power of -16 dBm incident to the electrodes, we obtain a Rabi frequency of 37.96(2) kHz and observe no significant damping in the contrast after approximately 40 Rabi oscillations. The microwave field produced by the electrode array is highly linearly polarized. For example, with the field set to drive π transitions, we are not able to resonantly drive the σ^- transition, even when the Rabi frequency on the π transition is increased to 133.7(1) kHz. Setting a conservative upper bound on Rabi frequency with which we drive the σ^- transition of 1 kHz, we extract the linear polarization purity of the microwave radiation emitted by the electrode array to be in excess of $10^4 : 1$. This enables high-fidelity control of the rotational states.

We probe higher rotational manifolds in the molecule using successive microwave transitions [80]. Here, we restrict ourselves to σ^+ transitions so that we always occupy a stretched hyperfine state in each rotational manifold. For example, in Fig. 4(a)(ii) we present spectroscopy of the transition $|1,1\rangle \rightarrow |2,2\rangle$. This is measured by first performing a π pulse on the transition $|0,0\rangle \rightarrow |1,1\rangle$ to prepare the molecule in $|1,1\rangle$ prior to the spectroscopy pulse. After the spectroscopy pulse, a third microwave pulse returns any molecules remaining in $|1,1\rangle$ back to $|0,0\rangle$ from which atom pairs can be recovered. Molecules that were excited to $|2,2\rangle$ during the spectroscopy pulse are not returned back to $|0,0\rangle$, resulting in atom pairs not being recovered. This is easily extended to higher manifolds; we generally prepare molecules in the stretched hyperfine state $|N,N\rangle$ with a series of N coherent π pulses before probing the transition $|N,N\rangle \rightarrow |N+1,N+1\rangle$ and returning molecules in $|N,N\rangle$ to $|0,0\rangle$. For example, in Fig. 4(a)(iii), we perform similar spectroscopy of the transition $|2,2\rangle \rightarrow |3,3\rangle$ with this procedure. As before, the measured frequencies for these transitions are within 10 kHz of the predicted frequencies indicated by the vertical lines in Fig. 4(b). Extension to more rotational states will allow the realization of a large number of synthetic lattice sites with fully controllable synthetic intersite tunnelings for engineering synthetic band structures [30].

V. MULTISTATE READOUT

Proposed quantum simulators composed of molecules often utilize the rotational states to encode pseudospins [5,84]. The detection of multiple rotational states of a molecule in a single iteration of the experiment would therefore prove highly valuable, particularly given the finite efficiency of forming bialkali molecules. For example, without the ability to readout multiple molecular states, it is impossible to distinguish between a molecule which is lost and a molecule in a spin state, which is not detected. In the following we describe a technique that

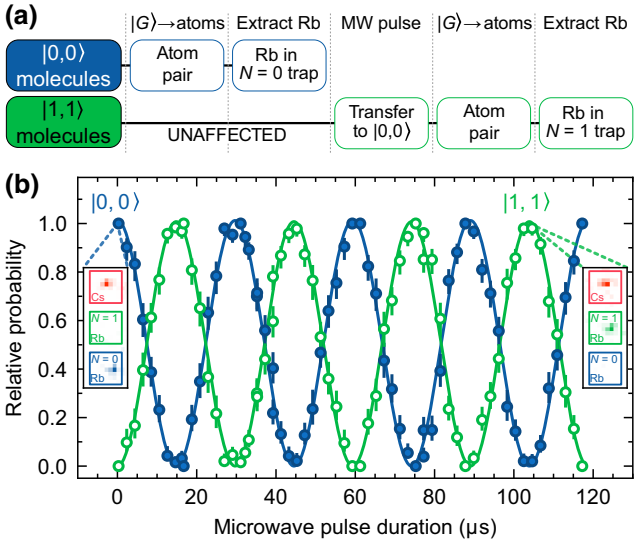

FIG. 5. Readout of multiple rotational states whilst driving the transition $|0,0\rangle \rightarrow |1,1\rangle$. (a) Flowchart of the detection procedure as described in the text. (b) Coherent transfer between $|0,0\rangle$ and $|1,1\rangle$. The Rabi frequency is 33.69(3) kHz and the fitted contrast is consistent with unity. The insets show the Cs (red) and Rb (green and blue) traps with example fluorescence images obtained from a molecule in states $|0,0\rangle$ (left) and $|1,1\rangle$ (right). Each point corresponds to the average across the four-molecule array with 100 experimental repetitions, where 24% of these runs satisfy the postselection criteria.

can be used to detect the rotational state of a molecule on a given site whilst avoiding errors caused by molecule loss.

We present an experimental scheme that maps the rotational state of the molecule onto atoms in spatially distinct tweezers, similar to the proposal of Ref. [85] where the state is mapped onto the atomic species. In our scheme, we detect the internal state of the molecule by mapping it onto the position of a Rb atom in the final fluorescence image. A flowchart of the detection scheme is shown in Fig. 5(a). We exploit the state specificity of the reverse STIRAP transfer; only molecules in state $|G\rangle$ are converted into atom pairs during the reverse STIRAP pulses and dissociation magnetic field sweeps. Molecules in excited rotational states are unaffected by these stages of the experimental routine. After atom pairs are recovered from molecules that were in state $|G\rangle$, they are separated and the Rb atoms are stored in a row of 817-nm tweezers. We then return to the usual operating magnetic field to transfer molecules in excited rotational states back to state $|G\rangle$ with a series of microwave pulses and repeat the dissociation steps. However, this time when separating the resultant atom pairs, we place the Rb atoms in a *different* row of 817-nm tweezers. After all the molecules have been dissociated into atom pairs, the magnetic field is reduced to 4.78 G and a final fluorescence image is taken. With this image, we can detect

the rotational state of the molecule prior to the readout procedure by observing which tweezer the Rb atoms populate. Using midsequence detection of Rb atoms, would allow this procedure to be repeated multiple times. This would enable many internal molecular states to be readout in a single experimental run, ideal for implementations of qudits [16] or quantum error correction using the internal states of the molecule [15].

This detection scheme allows us to mitigate the effects of noise in our experimental data. Such noise can result from fluctuations in the molecule formation efficiency or molecule loss, which reduces the recovery probability, P_r. We are also able to eliminate leakage errors that occur when molecules leave a chosen set of energy levels. The lowest rotational levels of RbCs have lifetimes exceeding 1000 s limited by black-body radiation [86]. Consequently, leakage errors due to off-resonant excitation during microwave transfers, for example, are much more likely than bit-flip errors for RbCs qubits. Using this detection scheme, we specify the energy-level subspace that we wish to readout with the choice of microwave pulses prior to converting the molecules back to atom pairs.

In Fig. 5(b) we present an example measurement performed with this detection scheme. Here, we drive a Rabi oscillation on the σ^+ transition between $|0,0\rangle$ (blue filled circles) and $|1,1\rangle$ (green empty circles) with a resonant microwave pulse applied to an array of four molecules. The Rabi frequency with which we drive the transition is 33.69(3) kHz. This avoids significant off-resonant excitation of the σ^- transition which is detuned by $-96(1)$ kHz at the magnetic field used in the experiment, as shown in Fig. 4(b)(i). After this pulse, molecules in $|0,0\rangle$ are converted back to atom pairs from which Rb atoms are moved to the "$N = 0$ detection" traps (insets, blue square). Molecules in $|1,1\rangle$ are then transferred back to $|0,0\rangle$ with a π pulse before we convert them back to atom pairs and deposit the Rb atoms into the "$N = 1$ detection" traps (insets, green square). Cs atoms always remain in the 1066-nm traps in which the molecules are formed (insets, red square). We postselect data to consider only experimental runs in which both a Cs atom and a Rb atom (in either of the two detection traps) are successfully recovered from an initial atom pair. This corresponds to 24% of the total number of runs for this dataset. The relative occupation of Rb atoms in the detection traps is used to infer the state of the molecule before the detection procedure. The fitted contrast of the Rabi oscillations is consistent with unity and we do not observe dephasing over the range of pulse durations shown here. The error bars in Fig. 5(b) represent the statistical uncertainties obtained from 100 repetitions of the experiment using an array of four molecules. The statistical uncertainty dominates over the systematic errors in the multistate readout scheme, which we estimate to be $\lesssim 2\%$ as detailed Appendix C.

VI. LOCAL CONTROL OF ROTATIONAL STATES

Controlling the rotational states of individual molecules within an array is essential for a range of applications. For example, preparing reactants in distinct rotational states facilitates studies of state-controlled quantum chemistry [87]. Additionally, certain quantum computation architectures using ultracold molecules require the selective excitation of molecules to perform single qubit gates [10] or to execute entangling gates between chosen pairs of molecules using microwave fields [14]. The targeted transfer of subsets of molecules into noninteracting states allows them to be shelved for midcircuit readout, enabling measurement-based quantum computation [88,89] or the study of measurement-induced phase transitions [90].

We demonstrate site-resolved control of the rotational state using an additional array of optical tweezers to address selected molecules. The additional tweezers cause a differential light shift between molecular states, altering the microwave transition frequency on the addressed sites. An example of this is shown in Fig. 6(a). In this measurement every other trap in an eight-trap array is addressed with an additional 817-nm tweezer, as indicated by the green rectangles in Fig. 6(b). The addressing

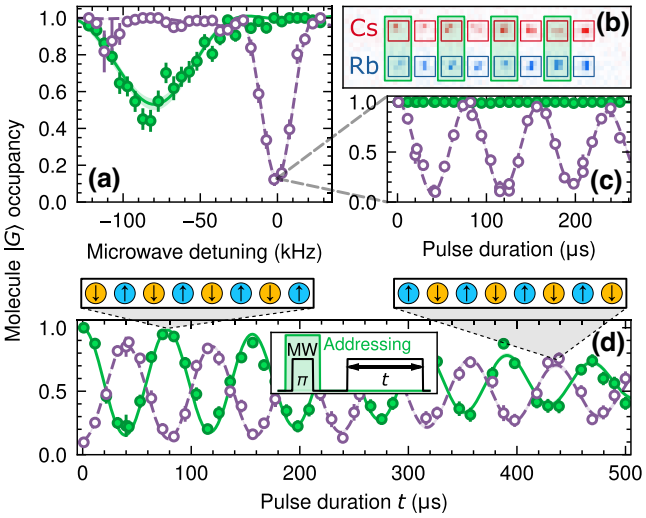

FIG. 6. Local control of rotational states in an array of molecules. (a) Selected molecules are addressed with an additional 817-nm tweezer that causes a light shift of the rotational transition in these molecules (green filled points) relative to the unaddressed molecules (purple empty points). (b) An image of the atoms that form the molecular array showing which sites are addressed (green highlight). (c) For a light shift of approximately -200 kHz applied to the addressed molecules, we drive Rabi oscillations in the unaddressed molecules only. (d) Preparation and manipulation of alternating spin chains of molecules. An initial π pulse transfers only unaddressed molecules to $|\uparrow\rangle$. The addressing is then removed to coherently rotate the spins of all molecules in the array.

tweezers are ramped up to an intensity of 2.18 kW/cm^2 after the molecules have been prepared in state $|G\rangle$. We then perform microwave spectroscopy on the array. Following this, the addressing light is removed such that all molecules are resonant with the microwave π pulses required for the multistate readout described earlier and the reverse STIRAP. The results in Fig. 6(a) show that the additional 817-nm tweezer light causes the frequency of the $|0,0\rangle \rightarrow |1,1\rangle$ transition to shift by $-80(2)$ kHz in the addressed molecules (green filled circles) relative to the unaddressed molecules (purple empty circles). The observed light shifts of the rotational transitions allow us to extract a value for the anisotropic polarizability of $\alpha^{(2)}_{817} = -2814(12) \times 4\pi\varepsilon_0 a_0^3$ for the 817 nm addressing tweezer. We note the increase in the size of the error bars for unaddressed molecules at a detuning of around -100 kHz in Fig. 6(a). This results from these molecules being excited on the σ^- transition such that the number of molecules remaining in the $\{|0,0\rangle, |1,1\rangle\}$ subspace from which we sample is greatly reduced.

When the induced light shift is much larger than the Rabi frequency of our chosen transition, we are able to drive transitions in *only* the unaddressed molecules. We demonstrate this in Fig. 6(c) where we increase the intensity of the addressing tweezers such that the light shift of the transition is approximately -200 kHz. We then apply microwave radiation that is resonant for the unaddressed molecules to drive a Rabi oscillation in only these molecules. After a π pulse, we observe no transfer of the addressed molecules out of state $|G\rangle$ and place a 1σ upper bound of 1.0% on the probability of driving an undesired excitation. We chose to target unaddressed molecules as fluctuations in the relative alignment of the trapping and addressing tweezers cause variations in the induced light shift and broaden the transitions of the addressed molecules.

We dynamically switch the addressing on and off during the experimental sequence to change between driving molecular transitions locally and globally. As an example, Fig. 6(d) shows the result of an experiment where we form an alternating spin chain of molecules with $|\downarrow\rangle \equiv |0,0\rangle$ and $|\uparrow\rangle \equiv |1,1\rangle$ and then drive Rabi oscillations in the whole array. The molecule formation stages initialize the array in $|\downarrow\rangle$. As before, half of the molecules in the array are then addressed with 817-nm light. A π pulse on the $|\downarrow\rangle \rightarrow |\uparrow\rangle$ transition is then driven in only the unaddressed molecules to prepare an alternating spin chain. We then remove the addressing light such that a second microwave pulse drives the rotational transition for all molecules in the array. This pulse rotates all the spins in the chain such that two adjacent molecules are always out of phase with each other. The dephasing evident in Fig. 6(d) is primarily caused by different trap depths across the array of eight molecules. This leads to a variation in the differential light shifts along the spin chain, such that the microwave field is not exactly resonant with all the molecules. In future work, we plan to address this problem by using an array of tweezers at a magic wavelength such that the differential light shift between the states $|\downarrow\rangle$ and $|\uparrow\rangle$ is eliminated [91].

VII. DETERMINISTIC ARRAY PREPARATION

We now demonstrate the preparation of defect-free arrays of molecules. The primary source of configurational entropy in our array is the finite conversion efficiency of atom pairs to molecules, which leads to some tweezers not containing molecules. We remove this entropy by detecting the traps where molecule formation failed using the procedure described in Sec. III C. Unlike the experiments presented thus far, in this experiment we perform the detection midsequence and use the information to rearrange molecules to occupy sites where formation failed.

Midsequence detection of molecule formation errors requires imaging Rb atoms at the magnetic field of 181.699(1) G used for STIRAP. At the normal imaging field of 4.78 G, the state $|G\rangle$ is no longer the lowest in energy and the hyperfine levels are more closely spaced. Imaging at high magnetic field therefore avoids potential loss of molecules to other states due to sweeping the magnetic field through numerous level crossings. Rb atoms in the detection array are imaged on the closed transition $(5s_{1/2}, f = 2, m_f = 2) \rightarrow (5p_{3/2}, f' = 3, m'_f = 3)$ [hereafter $(2,2)$ and $(3',3')$, respectively]. This approach has previously been used for nondestructive hyperfine-state readout of individually trapped Rb atoms [92,93]. As the Rb atoms are initially in the state $(5s_{1/2}, f = 1, m_f = 1)$ required for molecule formation, they are transferred to the state $(2,2)$ with microwave adiabatic rapid passage (ARP) before imaging, as illustrated in Fig. 1(d). Further details of the detection scheme are given in Appendix A.

Figure 7(a) shows a histogram of camera counts from a single Rb trap obtained using the high-field imaging procedure. During a rearrangement routine, trap occupancy is determined by comparing whether the observed counts are above or below a predefined threshold. The lines in Fig. 7(a) show the error in the occupancy assignment as this threshold is changed; the blue dashed line is the false-positive error ε_p and the red dashed line is the false-negative error ε_n. The black solid line is the average error probability ε, from which we extract a value of 3% when the threshold is optimized.

In Fig. 7(b) we verify the performance of the detection scheme by varying the ratio of tweezer intensities I_{817}/I_{1066} during the Rb extraction step. When I_{817} is too low, no Rb atoms are moved into the detection tweezers and a nonzero probability of detection corresponds to a false positive. Conversely, when I_{817} is high, all remaining Rb atoms are transferred to the detection tweezer and a probability below unity corresponds to a false negative. From the fit

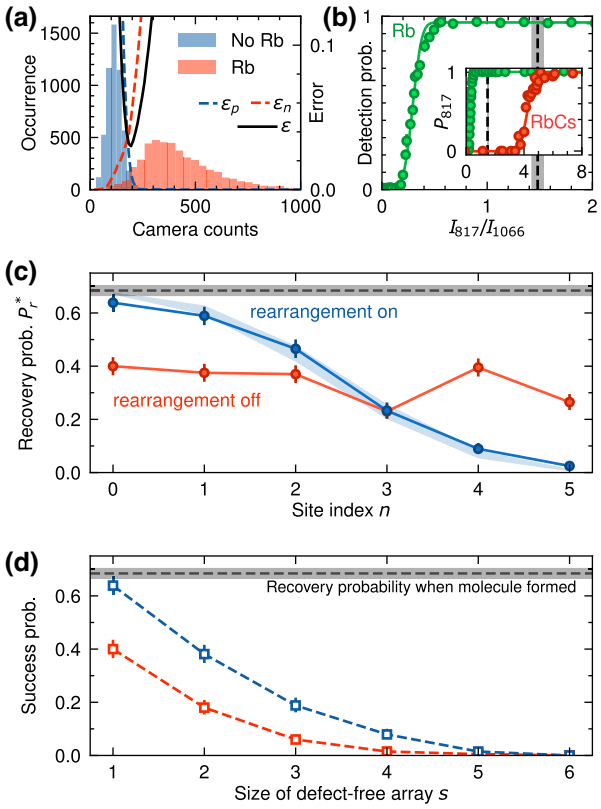

FIG. 7. Rearrangement of assembled molecules. (a) Histogram of camera counts obtained using high-field imaging of Rb atoms. Red (blue) data are counts obtained when an atom is (is not) present. The blue and red dashed lines are the probabilities of false-positive (ε_p) and false-negative (ε_n) errors, respectively, as the occupancy threshold is changed. The black solid line is the average error (ε). (b) The probability of detecting Rb in the detection trap as a function of the intensity ratio between the 817- and 1066-nm tweezers, I_{817}/I_{1066}, during the Rb extraction. The vertical dashed line indicates the value used in a typical sequence. The inset shows the probability P_{817} of pulling out Rb (green) and RbCs (red) with the 817-nm tweezer for higher values of I_{817}/I_{1066}. (c) The probability of molecule recovery P_r^* for each site n of the array. Blue (red) points show data with (without) molecule rearrangement for an initial array of six atom pairs. No postselection on successful molecule formation is performed; the black dashed line shows the measured recovery probability [0.68(2)] for a molecule that is formed and left in a single trap. The blue shaded region shows the prediction of a Monte Carlo simulation of the rearrangement. (d) The probability of successfully recovering defect-free arrays of size s, starting from site zero, with (blue) and without (red) rearrangement.

to Fig. 7(b) we find the combined procedure of extraction and imaging gives a false-positive rate of 0.7(1)% and a false-negative rate of 3.6(1)%. The latter is dominated by a approximately 2% probability for loss of the Rb atom prior to imaging. This value is consistent with the trap lifetime of Rb atoms in the experiment (approximately 30 s) and the duration of a typical experimental routine after Rb has been loaded (approximately 500 ms). The vertical dashed line in Fig. 7(b) shows the intensity ratio of 1.48(6) used for midsequence detection. This value is chosen to saturate the Rb detection fidelity whilst leaving molecules in their original traps, as shown in the inset.

We use the real-time information obtained from the high-field image to identify traps in which molecule formation was successful and rearrange the molecules to one side of the array. Molecule occupancy is assigned by inverting the measured Rb occupancy in the corresponding traps of the detection array. Molecules are then transferred from the 1066-nm array to an overlapping 817-nm array and unoccupied molecule traps are extinguished. Occupied molecule traps are then shuttled to one end of the array before the molecules are transferred back into the 1066-nm array.

We show the molecule recovery probabilities P_r^* obtained using this rearrangement scheme in Fig. 7(c). Here, we do *not* postselect statistics based on successful molecule formation, unlike in the experiments presented in earlier sections. For these measurements, exactly six atom pairs are prepared in the 1066-nm array, which we attempt to associate into molecules and transfer to state $|G\rangle$. For points with rearrangement enabled (blue), molecules are shuttled to the end of the array; for points with rearrangement disabled (red), the molecules are left in their original traps. We then reverse the association routine and image resultant atom pairs to determine P_r^*.

With rearrangement disabled, the molecule recovery across the array is approximately uniform with an average of 34(1)%. This is consistent with the 36(2)% that we expect from combining the typical molecule formation efficiency of 53(1)% with the molecule recapture probability $P_r = 68(2)\%$ obtained with this experimental routine when postselecting on successful molecule formation. We note that the molecule recapture probability is reduced from the values reported earlier in the paper due to increased time spent in the tweezers during imaging and the additional time required for calculating the rearrangement sequence. Variations in P_r^* (the probability that a molecule is formed *and* recovered) across the array primarily stem from variations in the probability of molecule *formation*. Molecules are formed only from atom pairs in the ground state of relative motion. Site-to-site differences in the intensities of the tweezers affect the cooling of the atoms to the motional ground state. Furthermore, angular misalignments across the array cause heating during the merging process. These effects cause variations in the probability of molecule formation, and therefore P_r^*, across the array.

When rearrangement is enabled, the average molecule recovery in the array remains 34(1)% but the distribution is no longer uniform, being weighted significantly towards the low-index sites in the array as intended. The observed recovery in the array agrees well with the prediction of a Monte Carlo simulation of the rearrangement, indicated

by the blue shaded region in Fig. 7(c). In this simulation, we populate the initial array of molecules by generating a random number, x_n, between 0 and 1 for each site in the array. If x_n is lower than the measured molecule formation efficiency for that site, then the site is deemed to be occupied. Once the initial occupancy of the array is determined, all molecules are shuttled to fill the traps with the lowest site indices. We assume that no molecules are lost during this process. This is repeated for 500 initializations of the array, and the average occupancy of each site is determined. The site occupancies are then scaled by the measured value of P_r. The shaded region shows the 1σ bounds on the simulation results, obtained by repeating it 500 times using different values of the molecule formation efficiency and P_r, both sampled from Gaussian distributions centered about their measured values with standard deviations equal to their experimental uncertainties.

Figure 7(d) shows the probability of successfully observing a defect-free array of size s. With rearrangement enabled, this probability scales as $(P_r)^s$ due to the loss of molecules prior to the final fluorescence image.

VIII. SCALING TO LARGER ARRAYS

Finally, we discuss scaling to larger arrays trapping a greater number of molecules. Currently, the performance of our rearrangement protocol is limited by laser power as this determines the initial number of molecules that can be formed. Using laser sources that produce 1 W of 1066-nm light and 100 mW of 817-nm light, we are able to assemble and rearrange an array of molecules starting from six atom pairs. However, at these wavelengths laser sources with output powers of 20 and 2 W, respectively, are readily available. Such lasers would allow a 20-fold increase in the array size in the short term and we note that higher-power laser sources exceeding 100 W [94,95] are available for further scaling in the long term.

In Fig. 8(a) we show the results of a Monte Carlo simulation of the expected rearrangement performance when using 120 atom pairs, corresponding to the anticipated 20-fold increase in laser power. The simulation is the same as that discussed in Sec. VII, but with a larger array of traps. The blue symbols show the predicted performance for $P_r = 68\%$; the value we measured in the rearrangement routine using six atom pairs. The green symbols show the performance that would be achieved if the molecule recovery probability were improved to $P_r = 88\%$. This latter value requires the infidelity in the hyperfine-state preparation to be reduced to 2% and the STIRAP efficiency increased to 99%. Both improvements are feasible in the near-term by changing the wavelength of the Rb tweezer to be further detuned (to reduce Raman scattering) and by suppressing phase noise on the STIRAP lasers using feed-forward techniques [96,97]. In both cases, the effect of nonunity P_r is to cause false-positive errors when

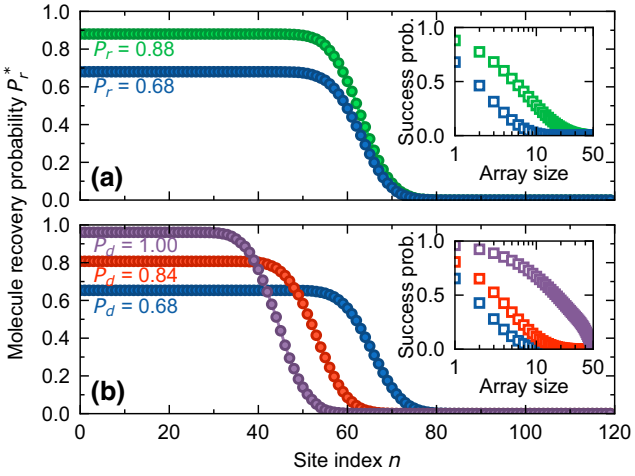

FIG. 8. Prospects for scaling the molecule rearrangement protocol to larger array sizes. The performance is simulated using the Monte Carlo method described in the text, starting with an array of 120 atom pairs. The main plots show the probability P_r^* of an atom pair being recovered from a molecule in site index n when *not* postselecting on molecule formation. The insets show the probability of measuring a defect-free array of a given size. (a) Rearrangement performance for different molecule recapture probabilities P_r using the detection scheme used in this work. (b) Rearrangement performance using direct detection of molecules in state $|G\rangle$ with probability P_d, rather than the detection of the failure to form molecules in state $|F\rangle$.

a molecule in state $|F\rangle$ is formed but subsequently lost, decreasing the average number of molecules in the array. The inset in Fig. 8(a) shows the probability of preparing a defect-free array, which reduces with array size s proportional to $(P_r)^s$, as we observed experimentally in Sec. VII.

We note that increasing the laser power available for tweezer generation will allow an increase in the number of rotational states that can be readout in a single run of the experiment. There is no fundamental limit to the number of states that can be readout with our detection scheme; we need only to have enough laser power to generate the required number of detection arrays.

Developing the capability to nondestructively detect molecules in state $|G\rangle$ would greatly enhance the prospect of large defect-free arrays of RbCs molecules. Currently, as the assembled molecules cannot be directly imaged, detection is limited to measuring only when a molecule has been formed. Consequently, we cannot correct for the subsequent loss of molecules. This leads to a significant drop in the probability of preparing a defect-free array when scaling to larger systems. To overcome this limitation, we propose to exploit the recently observed long-range interactions between molecules and Rydberg atoms [72] to detect molecules in state $|G\rangle$ directly. In such a scheme, atomic Rydberg excitation is blockaded when a ground-state molecule is present such that the presence of

a molecule can be inferred from the failure to excite to a Rydberg state [98–101].

In Fig. 8(b) we show the expected recovery of atom pairs from molecules in a sorted array using the proposed Rydberg-atom scheme. Here we use $P_r = 68\%$, the effect of which is now to reduce the average trap occupancy *before* rearrangement as detection can be performed after all the lossy molecule formation stages. The simulation is similar to before, but a trap is now occupied prior to rearrangement if $x_n < P_f P_r / \mathcal{F}_{\mathrm{STIRAP}}$, where $P_f = 53\%$ is the assumed molecule formation probability and $\mathcal{F}_{\mathrm{STIRAP}} = 96.4\%$ is the STIRAP fidelity. We show the results of simulations using different values of the molecule detection probability P_d. We expect P_d to be dominated by false-positive errors due to imperfect transfer to the atomic Rydberg state when no molecule is present. We incorporate this into the simulation by assigning each site with a second random number y_n between 0 and 1, such that if $y_n > P_d$ on an unoccupied site, we simulate a false-positive error in the detection by using this trap during the rearrangement even though it is unoccupied. As before, we repeat this simulation for 500 initializations of the array and determine the average occupancy of each site in the array. The limiting factor to atom pair recovery is now the reverse STIRAP transfer $\mathcal{F}_{\mathrm{STIRAP}}$ with which we scale the recovery probability of all the traps in the array. Nonunity detection fidelities P_d do not cause molecule loss but instead result in unoccupied molecule traps being inserted into the final array. This reduces the average occupancy of "filled" traps while increasing the length of the array that is "filled." The total number of molecules in the array is the same for all P_d shown here. These simulations suggest that a Rydberg excitation fidelity of $> 84\%$ (well below the approximately 99% that has been reported for Rb [43]) will enable the preparation of defect-free arrays of tens of assembled molecules.

The upgrades to our experiment described above will allow the formation of defect-free arrays of molecules comparable in size to those demonstrated with directly cooled molecules. For comparison, stochastic loading probabilities of approximately 35% are typical for an array of CaF molecules in optical tweezers [25]. The rearrangement of such molecules has been demonstrated to obtain defect-free arrays of up to 16 molecules with a probability > 0.6 for a reported single-particle rearrangement fidelity of 97.4(1)% and a state-preparation fidelity of 82.4(11)% [26]. In this work, the probability to convert an atom pair into a ground state molecule is 48(2)% and the direct detection of molecules in state $|G\rangle$ will allow for a rearrangement fidelity limited by the STIRAP fidelity [currently 96.4(1)%]. All molecules formed in this experiment occupy a single internal state. Furthermore, for assembled molecules such as RbCs, the molecule inherits the motional state of the center of mass of the atom pair from which it is assembled. As only atom pairs in the ground state of relative motion are converted into molecules, the formed molecules usually occupy the three-dimensional motional ground state. We estimate that this is true for approximately 66% of the molecules formed in our experiment [72]. This efficiency is comparable to the 54(18)% occupancy of the three-dimensional motional ground state achieved after Raman sideband cooling of CaF molecules in optical tweezers [102,103].

IX. CONCLUSION

In conclusion, we have established a suite of experimental techniques for enhanced control of individual ultracold molecules assembled from ultracold atoms confined in optical tweezer arrays. We have quantified the efficiency of each step in the method used to form RbCs molecules in optical tweezers and have described an adaptable technique for detecting molecule formation errors. We have demonstrated global and local control of multiple rotational states of individually trapped molecules and combined this with a technique for the detection of multiple rotational states in a single run of the experiment. Using midsequence detection of formation errors, we have demonstrated the rearrangement of assembled molecules to prepare defect-free arrays. Finally, we have discussed a feasible route to scaling to larger defect-free arrays of molecules.

The advances demonstrated here lay the foundation for new experiments in quantum science that exploit the rich internal structure and dipolar interactions of molecules [1–3]. We have developed a range of techniques for the control and readout of the rotational states of molecules using optical-tweezer arrays that can be readily extended beyond the two rotational states used in this work. This extension will facilitate the realization of synthetic dimensions [30] and qudits [16] with molecules. Furthermore, the combination of site-resolved control of rotational states with our scheme for the detection of multiple rotational states, allows for the local shelving of molecules outside the detected rotational subspace. This capability enables midcircuit measurements of a subset of molecules, which may be exploited to enhance precision measurements with molecules [104] or used for quantum information-processing applications, such as measurement-based quantum computation [88,89] and quantum error correction [105,106].

The data presented in this paper are available from Ref. [108].

ACKNOWLEDGMENTS

We thank Erkan Nurdun for developing the frequency stabilization system for the Rb high-field imaging laser and Jonathan Pritchard for valuable discussions regarding the implementation of high-field imaging. We thank

Stefan Spence for performing measurements of photoassociation of the weakly bound molecular states and Olivier Dulieu for helpful discussions about likely transition candidates. We acknowledge support from the UK Engineering and Physical Sciences Research Council (EPSRC) Grants No. EP/P01058X/1, No. EP/V047302/1, and No. EP/W00299X/1, UK Research and Innovation (UKRI) Frontier Research Grant No. EP/X023354/1, the Royal Society, and Durham University.

Note added.—Recently, we became aware of related work using NaCs molecules in the Ni group at Harvard University [107].

APPENDIX A: EXPERIMENTAL METHODS

The methods used in our experiment have been extensively described in previous works [48,55,56,72]. Here we provide an overview of recent upgrades relevant to this work.

1. STIRAP beams

The efficiency of one-way STIRAP transfer in our experiment has been increased from the previously reported value of 91(1)% [72] to the 96.4(1)% efficiency reported here by increasing the Rabi frequencies with which we couple to state $|E\rangle$. This has been achieved by amplifying the pump and Stokes beams with fiber amplifiers (both supplied by Precilasers) to have powers of approximately 44 mW and approximately 27 mW focused to $1/e^2$ beam waists of approximately 80 μm and approximately 70 μm at the molecules, respectively. With this we achieve a pump Rabi frequency of 493(5) kHz and a Stokes Rabi frequency of 876(4) kHz. Further increase of the Rabi frequencies beyond these values reduces the efficiency of the STIRAP transfer. We believe that the transfer efficiency at higher Rabi frequencies is limited by laser frequency noise [109,110] caused by servo bumps from frequency stabilization to a high-finesse optical cavity [111,112]. In the future, we plan to suppress this noise with feed-forward techniques [96,97].

2. High-field imaging

As described in the main text, to detect molecule formation errors midsequence we must image Rb atoms initially in the state $(5s_{1/2}, f = 1, m_f = 1)$ at a magnetic field of 181.699(1) G. Here we give further details of the microwave adiabatic rapid passage (ARP) and subsequent resonant imaging mentioned in Sec. VII.

The ARP transfer from $(1,1)$ to $(2,2)$ is implemented using a loop antenna mounted outside the vacuum chamber approximately 12 mm from the atoms confined in optical tweezers. With this antenna we produce microwave radiation that couples the states $(1,1)$ and $(2,2)$ with a Rabi frequency of 7.6(3) kHz. We use a magnetic field sweep of 72 mG in 2.5 ms to adiabatically transfer the atoms into $(2,2)$. For this Rabi frequency, the efficiency of the transfer is limited to 90% due to magnetic field noise. In future experiments we plan to increase the coupling strength to improve the transfer.

We then image the Rb atoms on the closed transition $(2,2) \rightarrow (3',3')$ with resonant σ^+ polarized light with a peak intensity of 10 I_{sat}. The use of the closed transition prevents atoms decaying to states that are dark to the imaging light due to the large Zeeman shifts. The imaging light is sourced from a dedicated laser, which is frequency stabilized relative to the main cooling laser with a beat note lock to be resonant with the imaging transition at the operating magnetic field of 181.699(1) G. The primary limitation to the achievable imaging fidelity is the loss of Rb atoms before the number of scattered photons that are detected is sufficient to differentiate occupied traps from the background. This loss is caused by the recoil momentum imparted by imaging photons heating atoms out of the traps. To combat this, we increase the peak depth of the tweezers to 2.5(1) mK × k_B. During the imaging procedure we modulate the imaging and trapping light in antiphase; this avoids light shifts caused by the deep trap, which would otherwise cause broadening of the signal histograms and loss from dipole-force fluctuations [113]. The duty cycle of the trapping (imaging) light is approximately 80% (10%) and we estimate that approximately 10^4 photons are scattered before the atoms are lost.

To enhance the preparation efficiency in (2,2) beyond the 90% achievable with ARP alone, and consequently improve the Rb detection fidelity, we implement additional optical pumping methods. We apply optical pumping light resonant with the $(1,1) \rightarrow (2',2')$ transition at 4.78 G, but off resonant at our magnetic field of 181.699(1) G. We also apply a microwave field resonant with the $(1,1) \rightarrow (2,2)$ transition during imaging to continuously pump atoms from the dark state $(1,1)$ to the bright state $(2,2)$. We find these steps pump $> 99\%$ of the atoms into the bright state for imaging.

APPENDIX B: MOLECULAR STATES

In the presence of externally applied optical and magnetic fields we resolve the hyperfine structure within each rotational manifold in RbCs. This hyperfine structure results from coupling between the rotational angular momentum and the nuclear spins of the constituent atoms ($i_{\mathrm{Rb}} = 3/2$ and $i_{\mathrm{Cs}} = 7/2$). This splits each $|N, M_N\rangle$ state into $(2i_{\mathrm{Rb}} + 1)(2i_{\mathrm{Cs}} + 1) = 32$ hyperfine states.

The magnetic field in our experiment is typically approximately 200 G, which is not high enough to decouple the rotational and nuclear angular momenta. As described in the main text, generally the only good quantum numbers that can be used to describe a given hyperfine sublevel are N and $M_F = M_N + m_{\mathrm{Rb}} + m_{\mathrm{Cs}}$. In the main

TABLE II. Rotational and hyperfine states of RbCs used in this work. We give the $|N, M_N\rangle$ label used in the main text, the corresponding $|N, M_F\rangle_k$ label, and the state compositions in a 1065.512-nm tweezer of intensity $I_{1066} = 3.07$ kW/cm^2 at a magnetic field of 181.699 G. The state components with $m_{\mathrm{Rb}} = 3/2$ and $m_{\mathrm{Cs}} = 7/2$ are shown in bold.

$\lvert N, M_N\rangle$	$\lvert N, M_F\rangle_k$	$\lvert N, M_N, m_{\mathrm{Rb}}, m_{\mathrm{Cs}}\rangle$
$\lvert 0,0\rangle \equiv \lvert G\rangle$	$\lvert 0,5\rangle_0$	$\lvert \mathbf{0,0,3/2,7/2}\rangle$
$\lvert 1,-1\rangle$	$\lvert 1,4\rangle_1$	$\mathbf{-0.827}\,\lvert \mathbf{1,-1,3/2,7/2}\rangle$ $-0.438\,\lvert 1,0,1/2,7/2\rangle$ $+0.293\,\lvert 1,1,-1/2,7/2\rangle$ $-0.196\,\lvert 1,0,3/2,5/2\rangle$ $-0.019\,\lvert 1,1,3/2,3/2\rangle$ $+0.011\,\lvert 1,1,1/2,5/2\rangle$
$\lvert 1,0\rangle$	$\lvert 1,5\rangle_0$	$\mathbf{-0.971}\,\lvert \mathbf{1,0,3/2,7/2}\rangle$ $+0.236\,\lvert 1,1,1/2,7/2\rangle$ $-0.039\,\lvert 1,1,3/2,5/2\rangle$
$\lvert 1,1\rangle$	$\lvert 1,6\rangle_0$	$\lvert \mathbf{1,1,3/2,7/2}\rangle$
$\lvert 2,2\rangle$	$\lvert 2,7\rangle_0$	$\lvert \mathbf{2,2,3/2,7/2}\rangle$
$\lvert 3,3\rangle$	$\lvert 3,8\rangle_0$	$\lvert \mathbf{3,3,3/2,7/2}\rangle$

text, we use the state labels $|N, M_N\rangle$ where mixed states are labeled with M_N of their component state with the largest probability amplitude. Neither of these labeling schemes is sufficient to identify a given hyperfine state uniquely. Therefore, here we use the labeling scheme of Blackmore *et al.* [80] where states are labeled by $|N, M_F\rangle_k$. Here k is an index enumerating states in order of increasing energy such that $k = 0$ is the lowest energy state for given values of N and M_F.

In Table II we list the hyperfine states used in this work. We give the label $|N, M_N\rangle$ used in the main text, the label $|N, M_F\rangle_k$ following the scheme of Blackmore *et al.*, and the full-state composition in the $|N, M_N, m_{\mathrm{Rb}}, m_{\mathrm{Cs}}\rangle$ basis. The state compositions are calculated for a molecule in a 1065.512-nm tweezer of intensity $I_{1066} = 3.07\,\mathrm{kW/cm^2}$ at a magnetic field of 181.699 G using the molecular constants and polarizabilities as described in the main text. The components of the $N = 1$ states to which we can couple with microwave radiation from state $|G\rangle$ have $m_{\mathrm{Rb}} = 3/2$ and $m_{\mathrm{Cs}} = 7/2$ and are highlighted in bold.

APPENDIX C: SYSTEMATIC ERRORS IN THE MULTISTATE READOUT PROTOCOL

The primary source of systematic error in the multistate readout scheme presented in Sec. V is the preferential loss of molecules in a particular rotational states. This cannot cause a molecule to be detected in the wrong rotational state, but can skew the ratio of the relative populations in the two states. To assess the impact of loss on the relative populations, we analyze the raw molecule recovery probabilities for the data presented in Fig. 5. The peak recovery probability of molecules in the state $|0, 0\rangle$ is 23.8(5)%, whereas the peak recovery probability of molecules in the state $|1, 1\rangle$ is 21.7(5)%. This corresponds to a relative recapture probability $r = 91(3)\%$ for molecules in state $|1, 1\rangle$ relative to molecules in the state $|0, 0\rangle$. The detection error is maximized to a value of $[1/(1 + r) - 1/2]$ when the true occupation of the two states is equal. For the results presented in Fig. 5, this corresponds to 2.3(8)%. As the true occupation of one of the states approaches unity, this resultant error decreases and eventually vanishes.

There are two main contributions to the preferential loss of molecules in the state $|1, 1\rangle$ that lead to the lower observed recovery probability. The first is loss due to scattering of the tweezer light during the time it takes to perform the readout of molecules in $|0, 0\rangle$. The duration of this stage is dominated by the approximately 10 ms required for the magnetic field to settle after separating the atom pairs that result from the dissociation of molecules in $|0, 0\rangle$. This leads to loss of approximately 1% of the molecules in $|1, 1\rangle$. Additionally, if the field has not completely settled, the efficiency of the second STIRAP transfer can be slightly reduced. The second source of loss is off-resonant excitation from $|1, 1\rangle$ to states with $N' = 2$ in the excited electronic manifold [114] when the Stokes light is applied during the readout of molecules in $|0, 0\rangle$.

Errors that would lead to the incorrect assignment of the molecular state are vanishingly rare. The selection rules governing the transitions used in STIRAP mean that the return transfer of molecules from the state $|1, 1\rangle$ is forbidden by parity [69], so these molecules cannot result in an atom in the $N = 0$ detection traps. For a molecule in the state $|0, 0\rangle$ to be detected as a molecule in $|1, 1\rangle$ would require it to remain in the state $|0, 0\rangle$ during the first dissociation stage and then be unaffected by the microwave π pulse used for readout of molecules in $|1, 1\rangle$. This is extremely unlikely.

[1] L. D. Carr, D. DeMille, R. V. Krems, and J. Ye, Cold and ultracold molecules: Science, technology and applications, New J. Phys. **11**, 055049 (2009).

[2] J. L. Bohn, A. M. Rey, and J. Ye, Cold molecules: Progress in quantum engineering of chemistry and quantum matter, Science **357**, 1002 (2017).

[3] T. P. Softley, Cold and ultracold molecules in the twenties, Proc. R. Soc. A: Math. Phys. Eng. Sci. **479**, 20220806 (2023).

[4] R. Barnett, D. Petrov, M. Lukin, and E. Demler, Quantum magnetism with multicomponent dipolar molecules in an optical lattice, Phys. Rev. Lett. **96**, 190401 (2006).

[5] A. V. Gorshkov, S. R. Manmana, G. Chen, J. Ye, E. Demler, M. D. Lukin, and A. M. Rey, Tunable superfluidity and quantum magnetism with ultracold polar molecules, Phys. Rev. Lett. **107**, 115301 (2011).

[6] M. Baranov, M. Dalmonte, G. Pupillo, and P. Zoller, Condensed matter theory of dipolar quantum gases, Chem. Rev. **112**, 5012 (2012).

[7] W. Lechner and P. Zoller, From classical to quantum glasses with ultracold polar molecules, Phys. Rev. Lett. **111**, 185306 (2013).

[8] M. L. Wall, K. R. A. Hazzard, and A. M. Rey, in *From Atomic to Mesoscale* (World Scientific, Singapore, 2015), Chap. 1, pp. 3–37.

[9] N. Y. Yao, M. P. Zaletel, D. M. Stamper-Kurn, and A. Vishwanath, A quantum dipolar spin liquid, Nat. Phys. **14**, 405 (2018).

[10] D. DeMille, Quantum computation with trapped polar molecules, Phys. Rev. Lett. **88**, 067901 (2002).

[11] S. F. Yelin, K. Kirby, and R. Côté, Schemes for robust quantum computation with polar molecules, Phys. Rev. A **74**, 050301(R) (2006).

[12] J. Zhu, S. Kais, Q. Wei, D. Herschbach, and B. Friedrich, Implementation of quantum logic gates using polar molecules in pendular states, J. Chem. Phys. **138**, 024104 (2013).

[13] K.-K. Ni, T. Rosenband, and D. D. Grimes, Dipolar exchange quantum logic gate with polar molecules, Chem. Sci. **9**, 6830 (2018).

[14] M. Hughes, M. D. Frye, R. Sawant, G. Bhole, J. A. Jones, S. L. Cornish, M. R. Tarbutt, J. M. Hutson, D. Jaksch, and J. Mur-Petit, Robust entangling gate for polar molecules using magnetic and microwave fields, Phys. Rev. A **101**, 062308 (2020).

[15] V. V. Albert, J. P. Covey, and J. Preskill, Robust encoding of a qubit in a molecule, Phys. Rev. X **10**, 031050 (2020).

[16] R. Sawant, J. A. Blackmore, P. D. Gregory, J. Mur-Petit, D. Jaksch, J. Aldegunde, J. M. Hutson, M. R. Tarbutt, and S. L. Cornish, Ultracold polar molecules as qudits, New J. Phys. **22**, 013027 (2020).

[17] R. V. Krems, Cold controlled chemistry, Phys. Chem. Chem. Phys. **10**, 4079 (2008).

[18] B. R. Heazlewood and T. P. Softley, Towards chemistry at absolute zero, Nat. Rev. Chem. **5**, 125 (2021).

[19] Y. Liu and K.-K. Ni, Bimolecular chemistry in the ultracold regime, Annu. Rev. Phys. Chem. **73**, 73 (2022).

[20] S. Schiller and V. Korobov, Tests of time independence of the electron and nuclear masses with ultracold molecules, Phys. Rev. A **71**, 032505 (2005).

[21] C. Chin, V. V. Flambaum, and M. G. Kozlov, Ultracold molecules: New probes on the variation of fundamental constants, New J. Phys. **11**, 055048 (2009).

[22] J. J. Hudson, D. M. Kara, I. J. Smallman, B. E. Sauer, M. R. Tarbutt, and E. A. Hinds, Improved measurement of the shape of the electron, Nature **473**, 493 (2011).

[23] V. Andreev, D. G. Ang, D. DeMille, J. M. Doyle, G. Gabrielse, J. Haefner, N. R. Hutzler, Z. Lasner, C. Meisenhelder, B. R. O'Leary, C. D. Panda, A. D. West, E. P. West, and X. Wu, A. C. M. E. Collaboration, Improved limit on the electric dipole moment of the electron, Nature **562**, 355 (2018).

[24] T. S. Roussy, L. Caldwell, T. Wright, W. B. Cairncross, Y. Shagam, K. B. Ng, N. Schlossberger, S. Y. Park, A. Wang, J. Ye, and E. A. Cornell, An improved bound on the electron's electric dipole moment, Science **381**, 46 (2023).

[25] Y. Bao, S. S. Yu, L. Anderegg, E. Chae, W. Ketterle, K.-K. Ni, and J. M. Doyle, Dipolar spin-exchange and entanglement between molecules in an optical tweezer array, Science **382**, 1138 (2023).

[26] C. M. Holland, Y. Lu, and L. W. Cheuk, On-demand entanglement of molecules in a reconfigurable optical tweezer array, Science **382**, 1143 (2023).

[27] B. Yan, S. A. Moses, B. Gadway, J. P. Covey, K. R. A. Hazzard, A. M. Rey, D. S. Jin, and J. Ye, Observation of dipolar spin-exchange interactions with lattice-confined polar molecules, Nature **501**, 521 (2013).

[28] J.-R. Li, K. Matsuda, C. Miller, A. N. Carroll, W. G. Tobias, J. S. Higgins, and J. Ye, Tunable itinerant spin dynamics with polar molecules, Nature **614**, 70 (2023).

[29] L. Christakis, J. S. Rosenberg, R. Raj, S. Chi, A. Morningstar, D. A. Huse, Z. Z. Yan, and W. S. Bakr, Probing site-resolved correlations in a spin system of ultracold molecules, Nature **614**, 64 (2023).

[30] B. Sundar, B. Gadway, and K. R. A. Hazzard, Synthetic dimensions in ultracold polar molecules, Sci. Rep. **8**, 3422 (2018).

[31] T. Langen, G. Valtolina, D. Wang, and J. Ye, Quantum state manipulation and science of ultracold molecules, arXiv:2305.13445v1.

[32] S. L. Cornish, M. R. Tarbutt, and K. R. A. Hazzard, Quantum computation and quantum simulation with ultracold molecules, arXiv:2401.05086v1.

[33] N. Schlosser, G. Reymond, I. Protsenko, and P. Grangier, Sub-poissonian loading of single atoms in a microscopic dipole trap, Nature **411**, 1024 (2001).

[34] N. Schlosser, G. Reymond, and P. Grangier, Collisional blockade in microscopic optical dipole traps, Phys. Rev. Lett. **89**, 023005 (2002).

[35] A. M. Kaufman and K.-K. Ni, Quantum science with optical tweezer arrays of ultracold atoms and molecules, Nat. Phys. **17**, 1324 (2021).

[36] D. Bluvstein, H. Levine, G. Semeghini, T. T. Wang, S. Ebadi, M. Kalinowski, A. Keesling, N. Maskara, H. Pichler, M. Greiner, V. Vuletić, and M. D. Lukin, A quantum processor based on coherent transport of entangled atom arrays, Nature **604**, 451 (2022).

[37] W. Lee, H. Kim, and J. Ahn, Three-dimensional rearrangement of single atoms using actively controlled optical microtraps, Opt. Express **24**, 9816 (2016).

[38] D. Barredo, S. de Léséleuc, V. Lienhard, T. Lahaye, and A. Browaeys, An atom-by-atom assembler of defect-free arbitrary two-dimensional atomic arrays, Science **354**, 1021 (2016).

[39] M. Endres, H. Bernien, A. Keesling, H. Levine, E. R. Anschuetz, A. Krajenbrink, C. Senko, V. Vuletic, M. Greiner, and M. D. Lukin, Atom-by-atom assembly of defect-free one-dimensional cold atom arrays, Science **354**, 1024 (2016).

[40] H. Labuhn, D. Barredo, S. Ravets, S. de Léséleuc, T. Macrì, T. Lahaye, and A. Browaeys, Tunable two-dimensional arrays of single Rydberg atoms for realizing quantum Ising models, Nature **534**, 667 (2016).

[41] H. Bernien, S. Schwartz, A. Keesling, H. Levine, A. Omran, H. Pichler, S. Choi, A. S. Zibrov, M. Endres, M. Greiner, V. Vuletić, and M. D. Lukin, Probing many-body

dynamics on a 51-atom quantum simulator, Nature **551**, 579 (2017).

[42] A. Browaeys and T. Lahaye, Many-body physics with individually controlled Rydberg atoms, Nat. Phys. **16**, 132 (2020).

[43] S. J. Evered, D. Bluvstein, M. Kalinowski, S. Ebadi, T. Manovitz, H. Zhou, S. H. Li, A. A. Geim, T. T. Wang, N. Maskara, H. Levine, G. Semeghini, M. Greiner, V. Vuletić, and M. D. Lukin, High-fidelity parallel entangling gates on a neutral-atom quantum computer, Nature **622**, 268 (2023).

[44] L. Anderegg, L. W. Cheuk, Y. Bao, S. Burchesky, W. Ketterle, K.-K. Ni, and J. M. Doyle, An optical tweezer array of ultracold molecules, Science **365**, 1156 (2019).

[45] C. M. Holland, Y. Lu, and L. W. Cheuk, Bichromatic imaging of single molecules in an optical tweezer array, Phys. Rev. Lett. **131**, 053202 (2023).

[46] N. B. Vilas, P. Robichaud, C. Hallas, G. K. Li, L. Anderegg, and J. M. Doyle, An optical tweezer array of ultracold polyatomic molecules, arXiv:2311.07529v1.

[47] W. B. Cairncross, J. T. Zhang, L. R. B. Picard, Y. Yu, K. Wang, and K.-K. Ni, Assembly of a rovibrational ground state molecule in an optical tweezer, Phys. Rev. Lett. **126**, 123402 (2021).

[48] D. K. Ruttley, A. Guttridge, S. Spence, R. C. Bird, C. R. Le Sueur, J. M. Hutson, and S. L. Cornish, Formation of ultracold molecules by merging optical tweezers, Phys. Rev. Lett. **130**, 223401 (2023).

[49] Y. Wu, S. Kolkowitz, S. Puri, and J. D. Thompson, Erasure conversion for fault-tolerant quantum computing in alkaline earth Rydberg atom arrays, Nat. Commun. **13**, 4657 (2022).

[50] P. Scholl, A. L. Shaw, R. B.-S. Tsai, R. Finkelstein, J. Choi, and M. Endres, Erasure conversion in a high-fidelity Rydberg quantum simulator, Nature **622**, 273 (2023).

[51] T. M. Graham, L. Phuttitarn, R. Chinnarasu, Y. Song, C. Poole, K. Jooya, J. Scott, A. Scott, P. Eichler, and M. Saffman, Mid-circuit measurements on a neutral atom quantum processor, arXiv:2303.10051.

[52] W. Huie, L. Li, N. Chen, X. Hu, Z. Jia, W. K. C. Sun, and J. P. Covey, Repetitive readout and real-time control of nuclear spin qubits in ^{171}Yb atoms, PRX Quantum **4**, 030337 (2023).

[53] J. W. Lis, A. Senoo, W. F. McGrew, F. Rönchen, A. Jenkins, and A. M. Kaufman, Midcircuit operations using the OMG architecture in neutral atom arrays, Phys. Rev. X **13**, 041035 (2023).

[54] M. A. Norcia *et al.*, Midcircuit qubit measurement and rearrangement in a ^{171}Yb atomic array, Phys. Rev. X **13**, 041034 (2023).

[55] R. V. Brooks, S. Spence, A. Guttridge, A. Alampounti, A. Rakonjac, L. A. McArd, J. M. Hutson, and S. L. Cornish, Preparation of one ^{87}Rb and one ^{133}Cs atom in a single optical tweezer, New J. Phys. **23**, 065002 (2021).

[56] S. Spence, R. V. Brooks, D. K. Ruttley, A. Guttridge, and S. L. Cornish, Preparation of ^{87}Rb and ^{133}Cs in the motional ground state of a single optical tweezer, New J. Phys. **24**, 103022 (2022).

[57] T. Takekoshi, L. Reichsöllner, A. Schindewolf, J. M. Hutson, C. R. Le Sueur, O. Dulieu, F. Ferlaino, R. Grimm, and H.-C. Nägerl, Ultracold dense samples of dipolar RbCs molecules in the rovibrational and hyperfine ground state, Phys. Rev. Lett. **113**, 205301 (2014).

[58] P. D. Gregory, M. D. Frye, J. A. Blackmore, E. M. Bridge, R. Sawant, J. M. Hutson, and S. L. Cornish, Sticky collisions of ultracold RbCs molecules, Nat. Commun. **10**, 3104 (2019).

[59] P. D. Gregory, J. A. Blackmore, S. L. Bromley, and S. L. Cornish, Loss of ultracold ^{87}Rb^{133}Cs molecules via optical excitation of long-lived two-body collision complexes, Phys. Rev. Lett. **124**, 163402 (2020).

[60] P. D. Gregory, J. A. Blackmore, F. M. D L. M. Fernley, S. L. Bromley, J. M. Hutson, and S. L. Cornish, Molecule–molecule and atom–molecule collisions with ultracold RbCs molecules, New J. Phys. **23**, 125004 (2021).

[61] J. T. Zhang, Y. Yu, W. B. Cairncross, K. Wang, L. R. B. Picard, J. D. Hood, Y.-W. Lin, J. M. Hutson, and K.-K. Ni, Forming a single molecule by magnetoassociation in an optical tweezer, Phys. Rev. Lett. **124**, 253401 (2020).

[62] T. Busch, B.-G. Englert, K. Rzażewski, and M. Wilkens, Two cold atoms in a harmonic trap, Found. Phys. **28**, 549 (1998).

[63] E. Hodby, S. T. Thompson, C. A. Regal, M. Greiner, A. C. Wilson, D. S. Jin, E. A. Cornell, and C. E. Wieman, Production efficiency of ultracold Feshbach molecules in bosonic and fermionic systems, Phys. Rev. Lett. **94**, 120402 (2005).

[64] T. Köhler, K. Góral, and P. S. Julienne, Production of cold molecules via magnetically tunable Feshbach resonances, Rev. Mod. Phys. **78**, 1311 (2006).

[65] C. Chin, R. Grimm, P. Julienne, and E. Tiesinga, Feshbach resonances in ultracold gases, Rev. Mod. Phys. **82**, 1225 (2010).

[66] T. Takekoshi, M. Debatin, R. Rameshan, F. Ferlaino, R. Grimm, H.-C. Nägerl, C. R. Le Sueur, J. M. Hutson, P. S. Julienne, S. Kotochigova, and E. Tiemann, Towards the production of ultracold ground-state RbCs molecules: Feshbach resonances, weakly bound states, and the coupled-channel model, Phys. Rev. A **85**, 032506 (2012).

[67] K. Bergmann, H. Theuer, and B. Shore, Coherent population transfer among quantum states of atoms and molecules, Rev. Mod. Phys. **70**, 1003 (1998).

[68] N. V. Vitanov, A. A. Rangelov, B. W. Shore, and K. Bergmann, Stimulated Raman adiabatic passage in physics, chemistry, and beyond, Rev. Mod. Phys. **89**, 015006 (2017).

[69] P. K. Molony, P. D. Gregory, Z. Ji, B. Lu, M. P. Köppinger, C. R. Le Sueur, C. L. Blackley, J. M. Hutson, and S. L. Cornish, Creation of ultracold ^{87}Rb^{133}Cs molecules in the rovibrational ground state, Phys. Rev. Lett. **113**, 255301 (2014).

[70] P. D. Gregory, P. K. Molony, M. P. Köppinger, A. Kumar, Z. Ji, B. Lu, A. L. Marchant, and S. L. Cornish, A simple, versatile laser system for the creation of ultracold ground state molecules, New J. Phys. **17**, 055006 (2015).

[71] P. K. Molony, P. D. Gregory, A. Kumar, C. R. Le Sueur, J. M. Hutson, and S. L. Cornish, Production of ultracold ^{87}Rb^{133}Cs in the absolute ground state: Complete characterisation of the STIRAP transfer, ChemPhysChem **17**, 3811 (2016).

[72] A. Guttridge, D. K. Ruttley, A. C. Baldock, R. González-Férez, H. R. Sadeghpour, C. S. Adams, and S. L. Cornish, Observation of Rydberg blockade due to the charge-dipole interaction between an atom and a polar molecule, Phys. Rev. Lett. **131**, 013401 (2023).

[73] P. D. Gregory, J. Aldegunde, J. M. Hutson, and S. L. Cornish, Controlling the rotational and hyperfine state of ultracold $^{87}Rb^{133}Cs$ molecules, Phys. Rev. A **94**, 041403(R) (2016).

[74] C. He, X. Nie, V. Avalos, S. Botsi, S. Kumar, A. Yang, and K. Dieckmann, Efficient creation of ultracold ground state $^{6}Li^{40}K$ polar molecules, arXiv:2310.03300.

[75] S. J. Spence, 2023, Ph.D. thesis (Durham University).

[76] O. Dulieu, (private communication).

[77] R. V. Brooks, 2022, Ph.D. thesis (Durham University).

[78] M. W. Gempel, T. Hartmann, T. A. Schulze, K. K. Voges, A. Zenesini, and S. Ospelkaus, Versatile electric fields for the manipulation of ultracold NaK molecules, New J. Phys. **18**, 045017 (2016).

[79] J. A. Blackmore, P. D. Gregory, J. M. Hutson, and S. L. Cornish, Diatomic-py: A Python module for calculating the rotational and hyperfine structure of $^{1}\Sigma$ molecules, Comput. Phys. Commun. **282**, 108512 (2023).

[80] J. A. Blackmore, P. D. Gregory, S. L. Bromley, and S. L. Cornish, Coherent manipulation of the internal state of ultracold $^{87}Rb^{133}Cs$ molecules with multiple microwave fields, Phys. Chem. Chem. Phys. **22**, 27529 (2020).

[81] P. D. Gregory, J. A. Blackmore, S. L. Bromley, J. M. Hutson, and S. L. Cornish, Robust storage qubits in ultracold polar molecules, Nat. Phys. **17**, 1149 (2021).

[82] J. A. Blackmore, R. Sawant, P. D. Gregory, S. L. Bromley, J. Aldegunde, J. M. Hutson, and S. L. Cornish, Controlling the ac Stark effect of RbCs with dc electric and magnetic fields, Phys. Rev. A **102**, 053316 (2020).

[83] R. Vexiau, D. Borsalino, M. Lepers, A. Orbán, M. Aymar, O. Dulieu, and N. Bouloufa-Maafa, Dynamic dipole polarizabilities of heteronuclear alkali dimers: optical response, trapping and control of ultracold molecules, Int. Rev. Phys. Chem. **36**, 709 (2017).

[84] A. Micheli, G. Brennen, and P. Zoller, A toolbox for lattice-spin models with polar molecules, Nat. Phys. **2**, 341 (2006).

[85] J. P. Covey, L. D. Marco, Ó. L. Acevedo, A. M. Rey, and J. Ye, An approach to spin-resolved molecular gas microscopy, New J. Phys. **20**, 043031 (2018).

[86] S. Kotochigova and E. Tiesinga, Ab initio relativistic calculation of the RbCs molecule, J. Chem. Phys. **123**, 174304 (2005).

[87] Y. Liu, M.-G. Hu, M. A. Nichols, D. Yang, D. Xie, H. Guo, and K.-K. Ni, Precision test of statistical dynamics with state-to-state ultracold chemistry, Nature **593**, 379 (2021).

[88] R. Raussendorf and H. J. Briegel, A one-way quantum computer, Phys. Rev. Lett. **86**, 5188 (2001).

[89] H. J. Briegel, D. E. Browne, W. Dür, R. Raussendorf, and M. Van den Nest, Measurement-based quantum computation, Nat. Phys. **5**, 19 (2009).

[90] M. P. Fisher, V. Khemani, A. Nahum, and S. Vijay, Random quantum circuits, Annu. Rev. Condens. Matter Phys. **14**, 335 (2023).

[91] P. D. Gregory, L. M. Fernley, A. L. Tao, S. L. Bromley, J. Stepp, Z. Zhang, S. Kotochigova, K. R. A. Hazzard, and S. L. Cornish, Second-scale rotational coherence and dipolar interactions in a gas of ultracold polar molecules, Nat. Phys. **20**, 415 (2024).

[92] M. Kwon, M. F. Ebert, T. G. Walker, and M. Saffman, Parallel low-loss measurement of multiple atomic qubits, Phys. Rev. Lett. **119**, 180504 (2017).

[93] M. Martinez-Dorantes, W. Alt, J. Gallego, S. Ghosh, L. Ratschbacher, Y. Völzke, and D. Meschede, Fast nondestructive parallel readout of neutral atom registers in optical potentials, Phys. Rev. Lett. **119**, 180503 (2017).

[94] C. Dixneuf, G. Guiraud, Y.-V. Bardin, Q. Rosa, M. Goeppner, A. Hilico, C. Pierre, J. Boullet, N. Traynor, and G. Santarelli, Ultra-low intensity noise, all fiber 365 W linearly polarized single frequency laser at 1064 nm, Opt. Express **28**, 10960 (2020).

[95] F. Wellmann, M. Steinke, P. Wessels, N. Bode, F. Meylahn, B. Willke, L. Overmeyer, J. Neumann, and D. Kracht, Performance study of a high-power single-frequency fiber amplifier architecture for gravitational wave detectors, Appl. Opt. **59**, 7945 (2020).

[96] L. Li, W. Huie, N. Chen, B. DeMarco, and J. P. Covey, Active cancellation of servo-induced noise on stabilized lasers via feedforward, Phys. Rev. Appl. **18**, 064005 (2022).

[97] Y.-X. Chao, Z.-X. Hua, X.-H. Liang, Z.-P. Yue, L. You, and M. K. Tey, Pound-Drever-Hall feedforward: Laser phase noise suppression beyond feedback, arXiv:2309.09759.

[98] E. Kuznetsova, S. T. Rittenhouse, H. R. Sadeghpour, and S. F. Yelin, Rydberg-atom-mediated nondestructive readout of collective rotational states in polar-molecule arrays, Phys. Rev. A **94**, 032325 (2016).

[99] M. Zeppenfeld, Nondestructive detection of polar molecules via Rydberg atoms, EPL **118**, 13002 (2017).

[100] K. Wang, C. P. Williams, L. R. B. Picard, N. Y. Yao, and K.-K. Ni, Enriching the quantum toolbox of ultracold molecules with Rydberg atoms, PRX Quantum **3**, 030339 (2022).

[101] C. Zhang and M. R. Tarbutt, Quantum computation in a hybrid array of molecules and Rydberg atoms, PRX Quantum **3**, 030340 (2022).

[102] Y. Lu, S. J. Li, C. M. Holland, and L. W. Cheuk, Raman sideband cooling of molecules in an optical tweezer array, arXiv:2306.02455.

[103] Y. Bao, S. S. Yu, J. You, L. Anderegg, E. Chae, W. Ketterle, K.-K. Ni, and J. M. Doyle, Raman sideband cooling of molecules in an optical tweezer array to the 3-D motional ground state, arXiv:2309.08706.

[104] T. Rosenband and D. R. Leibrandt, Exponential scaling of clock stability with atom number, arXiv:1303.6357.

[105] P. Shor, in *Proceedings of 37th Conference on Foundations of Computer Science* (IEEE, New York City, 1996), pp. 56–65.

[106] A. Steane, Multiple-particle interference and quantum error correction, Proc. R. Soc. A: Math. Phys. Eng. Sci. **452**, 2551 (1996).

[107] L. R. B. Picard, G. E. Patenotte, A. J. Park, S. F. Gebretsadkan, and K.-K. Ni, Site-selective preparation

and multi-state readout of molecules in optical tweezers, arXiv:2401.13659.

[108] D. K. Ruttley, A. Guttridge, T. R. Hepworth, and S. L. Cornish, Enhanced quantum control of individual ultracold molecules using optical tweezer arrays [dataset] (2024), https://doi.org/10.15128/r1j3860700f.

[109] P. A. Ivanov, N. V. Vitanov, and K. Bergmann, Effect of dephasing on stimulated Raman adiabatic passage, Phys. Rev. A **70**, 063409 (2004).

[110] W. Huang, W. Zhang, X. Du, and C. Guo, Population transfer under local dephasing, EPJ Quantum Technol. **9**, 34 (2022).

[111] S. de Léséleuc, D. Barredo, V. Lienhard, A. Browaeys, and T. Lahaye, Analysis of imperfections in the coherent optical excitation of single atoms to Rydberg states, Phys. Rev. A **97**, 053803 (2018).

[112] M. L. Day, P. J. Low, B. White, R. Islam, and C. Senko, Limits on atomic qubit control from laser noise, NPJ Quantum Inf. **8**, 72 (2022).

[113] M. Martinez-Dorantes, W. Alt, J. Gallego, S. Ghosh, L. Ratschbacher, and D. Meschede, State-dependent fluorescence of neutral atoms in optical potentials, Phys. Rev. A **97**, 023410 (2018).

[114] M. Debatin, 2013, Ph.D. thesis (University of Innsbruck).